



Nyathi, T. M., Fadlalla, M. I., Fischer, N., York, A. P.E., Olivier, E. J., Gibson, E. K., Wells, P. P. and Claeys, M. (2021) Support and gas environment effects on the preferential oxidation of carbon monoxide over Co₃O₄ catalysts studied in situ. *Applied Catalysis B: Environmental*, 297, 120450. (doi: [10.1016/j.apcatb.2021.120450](https://doi.org/10.1016/j.apcatb.2021.120450))

There may be differences between this version and the published version. You are advised to consult the published version if you wish to cite from it.

<http://eprints.gla.ac.uk/244280/>

Deposited on 17 June 2021

Enlighten – Research publications by members of the University of Glasgow
<http://eprints.gla.ac.uk>

Support and Gas Environment Effects on the Preferential Oxidation of Carbon Monoxide over Co_3O_4 Catalysts Studied *in situ*

Thulani M. Nyathi^a, Mohamed I. Fadlalla^a, Nico Fischer^a, Andrew P. E. York^b, Ezra J. Olivier^c, Emma K. Gibson^{d,e}, Peter P. Wells^{e,f,g}, Michael Claeys^{a,*}

^aCatalysis Institute and c*change (DSI-NRF Centre of Excellence in Catalysis), Department of Chemical Engineering, University of Cape Town, Rondebosch 7701, South Africa

^bJohnson Matthey Technology Centre, Sonning Common, Reading RG4 9NH, United Kingdom

^cCentre for High Resolution Transmission Electron Microscopy, Physics Department, Nelson Mandela University, PO Box 77000, Port Elizabeth, 6031, South Africa

^dSchool of Chemistry, Joseph Black Building, University of Glasgow, Glasgow G12 8QQ, United Kingdom

^eUK Catalysis Hub, Research Complex at Harwell, Rutherford Appleton Laboratory, Harwell, Oxon, OX11 0FA, United Kingdom

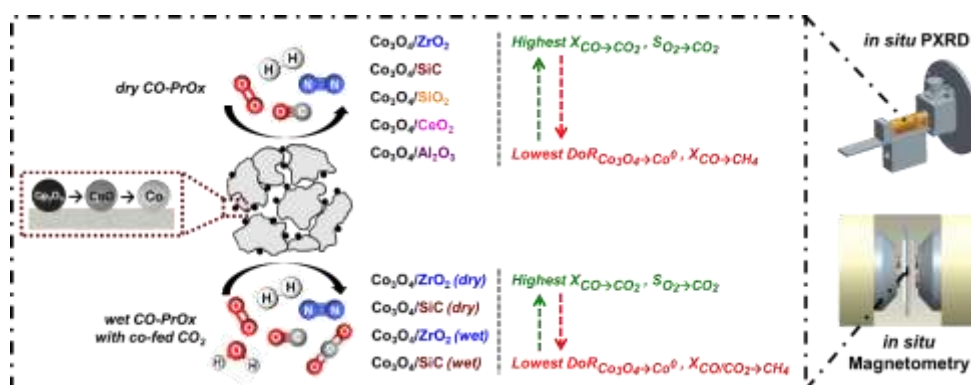
^fSchool of Chemistry, University of Southampton, University Road, Southampton SO17 1BJ, United Kingdom

^gDiamond Light Source Ltd., Harwell Science and Innovation Campus, Chilton, Didcot OX11 0DE, United Kingdom

Corresponding Author:

* Michael Claeys: michael.claeys@uct.ac.za

Graphical abstract



Highlights

- Supported Co_3O_4 catalysts evaluated under model and realistic CO-PrOx conditions using *in situ* PXRD and magnetometry.
- Weak nanoparticle-support interactions (as in $\text{Co}_3\text{O}_4/\text{ZrO}_2$) allow for high CO oxidation activity *via* the Mars-van Krevelen mechanism.
- Strong nanoparticle-support interactions (as in $\text{Co}_3\text{O}_4/\text{Al}_2\text{O}_3$) minimise Co^0 and associated CH_4 formation, but allow for undesired CoAl_2O_4 formation.
- Co-feeding H_2O suppresses CO oxidation and Co_3O_4 reduction, while co-feeding CO_2 results in methanation and the reverse water-gas shift over Co^0 .
- Bi-functional role required of support materials – enhancing CO oxidation activity/selectivity and stabilising the Co_3O_4 phase – is revealed.

Abstract

We have studied the effect of different supports (CeO_2 , ZrO_2 , SiC , SiO_2 and Al_2O_3) on the catalytic performance and phase stability of Co_3O_4 nanoparticles during the preferential oxidation of CO (CO-PrOx) under different H_2 -rich gas environments and temperatures. Our results show that $\text{Co}_3\text{O}_4/\text{ZrO}_2$ has superior CO oxidation activity, but transforms to Co^0 and consequently forms CH_4 at relatively low temperatures. The least reduced and least methanation active catalyst ($\text{Co}_3\text{O}_4/\text{Al}_2\text{O}_3$) also exhibits the lowest CO oxidation activity. Co-feeding H_2O and CO_2 suppresses CO oxidation over $\text{Co}_3\text{O}_4/\text{ZrO}_2$ and $\text{Co}_3\text{O}_4/\text{SiC}$, but also suppresses Co^0 and CH_4 formation. In conclusion, weak nanoparticle-support interactions (as in $\text{Co}_3\text{O}_4/\text{ZrO}_2$) favour high CO oxidation activity possibly *via* the Mars-van Krevelen mechanism. However, stronger interactions (as in $\text{Co}_3\text{O}_4/\text{Al}_2\text{O}_3$) help minimise Co^0 and CH_4 formation. Therefore, this work reveals the bi-functional role required of supports used in CO-PrOx, *i.e.*, to enhance catalytic performance and improve the phase stability of Co_3O_4 .

KEYWORDS: *CO-PrOx, Co₃O₄, support effects, gas environment effects, in situ characterisation*

1. Introduction

Cobalt(II, III) oxide (Co₃O₄) has been extensively studied as a CO oxidation catalyst in the absence of H₂, H₂O and CO₂, and exhibits very good catalytic activity. More specifically, the performance of Co₃O₄ can be influenced by a number of factors including; particle size [1], particle shape [2], preparation method [3] and type of support used [4]. There has also been growing interest in Co₃O₄ as a more affordable alternative to precious metals for the preferential oxidation of carbon monoxide (CO-PrOx) [5–9]. CO-PrOx is a promising process for the selective conversion of CO – *via* oxidation to CO₂ – in H₂-rich gas streams which are ultimately used for power generation in proton-exchange membrane fuel cells (PEMFCs). The CO content (0.5 – 2%) in the H₂-rich gas should be below 10 ppm (which corresponds to a CO conversion to CO₂ of 99.999% during CO-PrOx) to minimise the deactivation of the Pt-based anode catalyst of PEMFCs [10,11].

The H₂ (40 – 75%) in the CO-PrOx feed can negatively affect the CO₂ selectivity (based on the O₂ conversion) due to the oxidation of H₂ to form water. Moreover, recent *in situ* studies [5–9] have shown that Co₃O₄ reduces to CoO and metallic Co at elevated temperatures because of the abundant H₂. This phase change can negatively affect the CO₂ yield and selectivity during CO-PrOx, with the possibility of CH₄ formation over metallic Co. Although the formation of CH₄ also decreases the CO content in the feed, this involves consuming the valuable H₂ required in the PEMFC, and therefore, making methanation an unsuitable CO consuming route [10,11]. We have recently shown that co-feeding H₂O (*ca.* 10%) during CO-PrOx can decrease the CO oxidation activity/selectivity and the reducibility of unsupported Co₃O₄, while co-feeding CO₂ (*ca.* 10%) can result in higher H₂ conversions *via* methane formation and the reverse water-gas shift (WGS) over metallic Co, which is also undesired [9].

The use of support materials for anchoring active nanoparticles is a common practice in heterogeneous catalysis as it helps with dispersing the nanoparticles and with minimising their growth *via* sintering at high reaction temperatures [12]. Support materials can also help stabilise the chemical phase (*e.g.*, the oxide) of the nanoparticles depending on the nature and/or strength of the nanoparticle-support interactions (NPSI) [4,8,13–18]. We have demonstrated this phenomenon under model or dry CO-PrOx conditions (*i.e.*, in the absence

of H₂O and CO₂) with two Co₃O₄/Al₂O₃ catalysts, mainly prepared *via* the reverse microemulsion technique but using two different supporting methods [8]. Contacting the Al₂O₃ support with cobalt hydroxide (Co(OH)_x) suspended/confined within the water droplets of the reverse microemulsion, leads to the development of strong NPSI. However, contacting the support with pre-calcined Co₃O₄ nanoparticles in water (*i.e.*, not in a reverse microemulsion) weakens or limits the development of the NPSI. As a result of the weak interactions, high CO oxidation activity and selectivity (possibly *via* the Mars-van Krevelen (MvK) mechanism [1,19–21]) was observed over the Co₃O₄ phase below 225 °C, but at higher temperatures, the Co₃O₄ reduced to the less active/selective CoO and metallic Co phases. Strong NPSI improved the phase stability of Co₃O₄ over a wide temperature range, despite exhibiting lower CO oxidation activity due to the decreased (surface) reducibility of Co₃O₄, which resulted in a less effective MvK mechanism.

Following from our previous work, we have now considered different support materials – oxidic (*viz.*, CeO₂, ZrO₂, SiO₂ and Al₂O₃) and non-oxidic (*viz.*, SiC) – for anchoring Co₃O₄ nanoparticles and thereafter, evaluated the supported catalysts under “dry” and “wet” CO-PrOx conditions (with the latter condition representing a realistic reaction environment containing H₂O and CO₂). The kind of support and the nature/strength of the NPSI are some of the factors that can influence the catalytic performance and phase stability of Co₃O₄ [4,8,15]. The materials CeO₂ and ZrO₂ [15,22] are commonly used as supports for CO-PrOx catalysts as they allow for good activity to be achieved over the supported metal or metal oxide nanoparticles. However, the reducibility of the oxide nanoparticles can be high over these two supports, possibly as a consequence of the relatively weak NPSI [15,23].

The supports SiO₂ and Al₂O₃ are known to stabilise oxide nanoparticles under reducing conditions through the existence of strong NPSI. As a consequence of the strong interactions, these supports can sometimes react with foreign metal ions (such as Coⁿ⁺) in H₂-H₂O mixtures at relatively high temperatures to form irreducible mixed metal oxides (such as Co₂SiO₄ and CoAl₂O₄) [13,14,24,25]. The use of SiC as a support can help prevent the loss of Co species *via* mixed metal oxide formation as this support is inert in comparison [26]. Unlike CeO₂ and ZrO₂, the materials SiC, SiO₂ and Al₂O₃ have been studied to a lesser extent as CO-PrOx supports in terms of their effect on catalytic activity, selectivity and phase stability, which justifies their inclusion in the present study.

Two complementary *in situ* techniques – a powder X-ray diffraction (PXRD) capillary reaction cell [27–29] and a sample magnetometer [29,30] – were used in this study to monitor the phase changes of supported Co_3O_4 during dry and wet CO-PrOx conditions. The *in situ* characterisation was coupled with on-line product analysis *via* gas chromatography (GC). Consolidation of the gas product analysis and *in situ* characterisation helped identify the gas phase reactions possible under the chosen CO-PrOx conditions, and to associate these reactions with the responsible Co-based phase. For the first time, this work reveals the important bi-functional role required of catalyst support materials being used in the CO-PrOx reaction, *i.e.*, to enhance catalytic performance and improve the phase stability of Co_3O_4 . This was achieved by considering a variety of supports for anchoring Co_3O_4 nanoparticles and evaluating the supported catalysts under model (*i.e.*, “dry”) and realistic (*i.e.*, “wet”) CO-PrOx conditions. This is in contrast with our previous publications where one support (either Al_2O_3 [6,8] or SiO_2 [7]) was studied under model reaction conditions only.

2. Method

2.1. Catalyst preparation

The supported catalysts were prepared using incipient wetness impregnation of the pre-calcined (at 300 °C) CeO_2 nanopowder (US Nano), ZrO_2 nanopowder (US Nano), fumed SiO_2 (AEROSIL 150, Evonik Industries), Al_2O_3 (PURALOX SCCa 5-150, SASOL Germany), as well as crushed and sieved (< 150 μm) mesoporous SiC (purchased as 1 mm extrudates, SiCAT Sarl), with an aqueous solution of 1.2 g of $\text{Co}(\text{NO}_3)_2 \cdot 6\text{H}_2\text{O}$ (reagent grade 98% purity, Sigma-Aldrich South Africa) for every 1 mL of deionised water. The pore volume of each bare support, which was used to guide the impregnation, can be found in Table 1. The targeted Co_3O_4 loading was 10 wt.-% (equivalent to 7.3 wt.-% Co) on all support materials. The impregnated supports were dried overnight at 60 °C under a N_2 flow (50 mL(NTP)/min), and then annealed for 60 minutes at 350 °C (heating rate: 2 °C/min) under the same gas flow at atmospheric pressure [31] in a glass calcination tube (I.D.: 15 mm, length: 240 mm; Lasec SA). In cases where a second impregnation step was required (that is for CeO_2 , ZrO_2 and SiC), this was done using the calcined material obtained after the first impregnation. These three supports had relatively low pore volumes, *i.e.*, < 0.2 cm^3/g (also see Table 1).

The fresh and spent supported Co_3O_4 catalysts were characterised *ex situ* using powder X-ray diffraction (PXRD), scanning transmission electron microscopy coupled with electron energy loss spectroscopy (STEM-EELS), nitrogen physisorption, inductively coupled plasma-optical emission spectroscopy (ICP-OES), and X-ray absorption spectroscopy (XAS). The measurement and data processing details pertaining to each *ex situ* technique can be found in the “*Ex situ* characterisation” section of the Supplementary Information.

2.2. *In situ* catalyst characterisation and evaluation

2.2.1. Reduction studies

The reduction of the supported catalysts was conducted in a gas flow of 50% H_2 in N_2 at atmospheric pressure using a capillary-based reaction cell (developed at the University of Cape Town (UCT), South Africa) [27–29]. The cell uses a fixed-bed capillary reactor, made from borosilicate glass (length: 75 mm, wall thickness: 0.02 mm, O.D.: 1.0 mm (Capillary Tube Supplies LTD, UK)), through which gas can be flowed using a mass flow controller (Brooks Instruments). Due to the different densities of the supported catalysts, different amounts (in mass) of catalyst were used to fill the 15 mm isothermal zone along the middle of the capillary reactor. The gas flow rates were also varied to maintain a gas-hourly space velocity (GHSV) of 60000 mL(NTP)/g Co_3O_4 /hr. The amounts of catalyst and gas flow rates used for the reduction experiments can be found in Tables S1 and S2, respectively. A K-type thermocouple (Unitemp, South Africa), with a diameter of 0.5 mm, was placed inside the capillary reactor with its tip in contact with the end of the catalyst bed. At this point, both the loaded reactor and the thermocouple are positioned horizontally in the PXRD cell.

The cell was mounted on a Bruker D8 Advance Laboratory X-ray diffractometer, equipped with a Mo source ($\lambda_{\text{K}\alpha 1} = 0.7093 \text{ \AA}$) and a position-sensitive detector (VANTEC, Bruker AXS), to allow for PXRD patterns to be recorded during the reduction. The diffractometer was operated at 50 kV and 35 mA; and the optics were set to parallel beam geometry to minimise possible peak shifts due to sample height differences. The loaded capillary reactor was heated from 50 to 450 °C (at a rate of 1 °C/min), and thereafter, the temperature was held at 450 °C for 2 hours. A 2θ measurement window of 15 – 30° (or a $1/d$ range of 0.37 – 0.73 \AA^{-1}), a step size of 0.019° (4.7 x 10⁻⁴ \AA^{-1}), and a time per step of 0.20 seconds were applied (total scan

time: 4 minutes and 2 seconds, with an added 58-second delay between scans). PXRD patterns were recorded every 5 minutes throughout each reduction experiment.

All the *in situ* diffraction patterns recorded during reduction were compared with the known diffraction patterns found in the International Centre for Diffraction Data (ICDD) Powder Diffraction File-2 (PDF-2) database [32] to determine the chemical and crystallographic phases present. Rietveld refinement was carried out using the TOPAS 5.0 software package (Bruker AXS) [33] to quantify the Co-based phases present in terms of their relative weight fraction and volume-based average crystallite size. The details of the refinement can be found in the section “Rietveld refinement protocols” of the Supplementary Information. Similar analytical approaches (as described in the section “Rietveld refinement protocols”) were used for obtaining quantitative information from the *ex situ* PXRD patterns acquired for all fresh catalysts, and the *in situ* patterns acquired during CO-PrOx (*vide infra*).

Conventional H₂-TPR was also conducted on the bare supports and the supported catalysts. A sample of 0.1 g was placed between two pieces of quartz wool in a U-shaped quartz reactor. The reduction was carried out in a Micromeritics AutoChem 2920 instrument, equipped with a thermal conductivity detector (TCD) for measuring the H₂ consumption. The sample was firstly dried by heating the reactor from room temperature to 120 °C at a rate of 10 °C/min under a flow of Ar (10 mL(NTP)/min), and then keeping the temperature at 120 °C for 60 minutes. Thereafter, the temperature was decreased to 60 °C before switching the gas flow to 5% H₂ in Ar (50 mL(NTP)/min). Under this reducing gas mixture, the reactor was heated to 920 °C at a rate of 10 °C/min, which was kept for 10 minutes before cooling to room temperature. The H₂ consumption was measured every 0.1 minutes (6 seconds) between 60 and 920 °C after introducing the reducing gas. The degree of reduction (DoR) of each bare support or supported Co₃O₄ catalyst to the corresponding metal or metal oxide phase (where possible) was calculated based on the instrument calibration performed using different known amounts of Ag₂O (also see Equations S1 – S4).

2.2.2. Catalyst evaluation under different CO-PrOx reaction environments

The prepared catalysts were evaluated under dry and wet CO-PrOx conditions (with the latter also involving H₂O and CO₂ co-feeding) in the PXRD cell described above, and in an *in situ* sample magnetometer (developed by UCT and SASOL, South Africa) [29,30]. The

magnetometer uses a ½-inch stainless steel fixed-bed reactor (I.D.: 9.7 mm) that is placed vertically between two pole caps of a current-controlled electro-magnet (maximum external field strength: 2 T (or 20 kOe), Bruker Analytik GmbH). The use of PXRD allows for the detection of Co₃O₄, CoO and metallic Co; whereas using the magnetometer only enables the detection of metallic Co as it is the only ferromagnetic Co-based phase [34] among those that can be formed in the current study. The other Co-based phases are antiferromagnetic [35–37] – see detailed definitions in the Supplementary Information. Amounts of metallic Co that are as little as 0.23 mg (*ca.* 0.1 wt.-% in this study) can be detected using the magnetometer [8], while PXRD requires relative amounts of metallic Co (and of other materials) that are above 2 – 3 wt.-% (and above 2 – 3 nm in terms of crystallite size) for adequate detection. PXRD also requires crystalline material, whereas the detection of ferromagnetic material in the magnetometer is virtually independent of crystallinity.

PXRD patterns and magnetisation measurements (at 2 T) were recorded every 5 minutes in the separate *in situ* instruments. The scan parameters (*i.e.*, 2 θ (or 1/d) range, step size, and time per step) used for the PXRD-based reduction studies were also applied for the PXRD-based CO-PrOx reactions. The data from the magnetisation measurements were used to calculate the DoR of Co₃O₄ to metallic Co using Equation 1 (which is also Equation S5). The feed for dry CO-PrOx composed of 1% CO, 1% O₂, 50% H₂ and 48% N₂; while the feed for wet CO-PrOx with co-fed CO₂ included 1% CO, 1% O₂, 46% H₂, 10% H₂O, 9% CO₂ and 33% N₂. The gas feed was flowed at a GHSV of 60000 mL(NTP)/g_{Co₃O₄}/hr at atmospheric pressure in each *in situ* instrument. However, different amounts of catalyst and gas flow rates (especially in the PXRD cell) were used due to the different sample densities – see Tables S1 and S2. The loaded reactor in each instrument was heated from 50 to 450 °C during dry CO-PrOx, and from 100 to 450 °C during wet CO-PrOx with co-fed CO₂ (to prevent the condensation of water below 100 °C); at a rate of 1 °C/min and while holding the temperature at every 25 °C for 60 minutes. To measure the temperature of the catalyst bed during the magnetometry-based experiments, a non-magnetic N-type thermocouple (diameter: 3.2 mm, length: 304.8 mm, Omega) was placed vertically inside the reactor, with its tip situated in the middle of the catalyst bed.

$$\text{DoR}(\%) = \frac{M_{\text{sample}} \cdot 0.1 \text{ g}}{M_{\text{calibration}} \cdot X_{\text{loading}} \cdot m_{\text{unreduced sample}}} \times 100 \quad (1)$$

M_{sample} is the sample magnetisation (in emu) at any temperature within the temperature window used in this study; and $M_{calibration}$ is the corresponding magnetisation of metallic Co (in emu) from the calibration curve in Figure S1 at the same temperature. $X_{loading}$ is the metal loading as determined from ICP-OES, and $m_{unreduced\ sample}$ is the mass of the unreduced supported sample (in g) loaded into the reactor.

The reactor effluent gas from the CO-PrOx experiments was sampled on-line every 5 minutes using a Varian CP 4900 micro-GC (Agilent) fitted with TCDs for detecting CO, O₂, H₂, CO₂, CH₄ and N₂ in three different columns (see Table S3 for the identity of the detectors and the full set of parameters applied to achieve gas separation). The water produced or consumed during the experiments could not be quantified as it was condensed in a cold trapping vessel before the other gases were sampled by the micro-GC. The chromatographic analysis was operated using the Varian Galaxie Chromatography Data System (version 1.9.3.2). The relevant peak areas in each chromatogram were used to calculate the volumetric flow rates of each eluting gas using Equations S6 and S7. Furthermore, the normalised gas outlet flow rates (Equation S8), conversions (Equations S9 – S12) and selectivities (Equation S13) were calculated from the volumetric flow rates. From these equations and the knowledge of the reactions that can occur under each reaction condition, the formation or consumption of water could be inferred.

3. Results and Discussion

3.1. *Ex situ* catalyst characterisation

PXRD analysis was used to confirm the chemical and crystallographic phase of the Co-based species in all fresh supported catalysts. The full diffraction patterns of the bare supports and the supported catalysts can be found in Figure S3 and S4, respectively. All the expected Co₃O₄ reflections are present in the diffraction pattern of Co₃O₄/SiO₂ due to the amorphous nature of SiO₂. The diffraction patterns for the ZrO₂-, SiC- and Al₂O₃-supported catalysts show some of the reflections from Co₃O₄, despite the crystalline nature of these supports, which causes some of the reflections from each support to overlap with those from Co₃O₄. The PXRD pattern of Co₃O₄/CeO₂ barely shows the main Co₃O₄(3 1 1) reflection at $1/d = 0.41 \text{ \AA}^{-1}$ (Figure S4(b)).

However, this is common for $\text{Co}_3\text{O}_4/\text{CeO}_2$ catalysts with a loading of 10 wt.-% or lower [38,39]. In the work by Guo and Liu [38], loadings higher than 10 wt.-% were required to adequately detect the Co_3O_4 phase.

At this stage, we propose that the limited detection of Co_3O_4 in the $\text{Co}_3\text{O}_4/\text{CeO}_2$ catalyst could be due to the high X-ray mass absorption coefficient of Ce ($563.3 \text{ cm}^2/\text{g}$) compared to Zr ($287.3 \text{ cm}^2/\text{g}$), Co ($250.7 \text{ cm}^2/\text{g}$), Si ($143.9 \text{ cm}^2/\text{g}$), Al ($113.3 \text{ cm}^2/\text{g}$), O ($27.1 \text{ cm}^2/\text{g}$) and C ($10.5 \text{ cm}^2/\text{g}$) [40]. Note that the reported coefficients are based on the X-ray photon energy of 6930.2 eV ($\lambda_{\text{Co}, \text{K}\alpha 1} = 1.78897 \text{ \AA}$), which is the energy of the X-rays used for the *ex situ* PXRD measurements. The high absorption of the X-rays by CeO_2 (or Ce) could have limited the interaction of the Co_3O_4 particles with the X-rays, especially if the particles are located in the pores of CeO_2 (a result of using incipient wetness impregnation [41,42]).

The average crystallite size of Co_3O_4 varies within the narrow range of 13.0 and 15.2 nm among the catalysts prepared (see Table 1). The relative Co_3O_4 weight fraction varies between 9.8 and 11.3 wt.-% for the ZrO_2 -, SiC- and Al_2O_3 -supported catalysts, and is close to the targeted loading of 10 wt.-%. The weight fraction of Co_3O_4 in the SiO_2 -supported catalyst could not be calculated since SiO_2 is amorphous. The small crystallite size and low relative weight fraction of Co_3O_4 ($7.7 \pm 0.2 \text{ nm}$ and $6.5 \pm 0.8 \text{ wt.-%}$, respectively – see Table 1) in the $\text{Co}_3\text{O}_4/\text{CeO}_2$ catalyst could be a result of the very low intensity of the Co_3O_4 reflections (or absence thereof) in the acquired full diffraction pattern.

Ex situ XAS was used to analyse the fresh $\text{Co}_3\text{O}_4/\text{CeO}_2$ sample following the inconclusive PXRD measurement. The normalised XANES (X-ray absorption near edge structure) spectrum of this fresh sample is shown in Figure S5(a), together with the spectrum of the Co_3O_4 reference. The two spectra have a common main edge at 7721 eV and the XANES features after the edge are similar between the two samples. Furthermore, the oscillations in the EXAFS region confirm Co_3O_4 as the bulk average Co-based phase present in the fresh catalyst (Figure S5(b)), since CoO and metallic Co exhibit oscillations that are out of phase with those of the fresh catalyst (Figure S6).

The distribution and size of the fresh cobalt-bearing particles over each support was studied using STEM-EELS. The bright-field micrograph and the corresponding Co map (generated based on the Co L-edge) of each catalyst are shown in Figure S7. The Co maps show several single Co-bearing particles of different irregular shapes, as well as Co-bearing clusters/agglomerates in each sample. Nonetheless, the size of the single particles was

measured to obtain a number-based size distribution for each fresh catalyst (Figure S8). Table 1 shows the number- and volume-based average size of Co_3O_4 derived from the particles counted and it can be seen that the catalysts have a number-based average particle size that is between 9.9 and 16.2 nm. On the other hand, the volume-based STEM average sizes are generally larger than the volume-based PXRD average sizes, which may suggest the presence of smaller crystalline domains (measured using PXRD but not STEM due to the low magnification/resolution) that make up the larger Co_3O_4 particles measured in the STEM micrographs [43].

Nitrogen physisorption was performed on all bare and Co_3O_4 -loaded supports to determine their physical characteristics in terms of surface area and porosity. These parameters give an indication on the success of the incipient wetness impregnation method as most of the Co_3O_4 nanoparticles were intended to be present in the “pores” of each support after calcination. Table 1 includes a summary of the BET surface areas and the BJH pore volumes of each sample. In general, the surface area and pore volume after catalyst preparation is lower when compared with the bare support. However, the surface area of $\text{Co}_3\text{O}_4/\text{ZrO}_2$ and the pore volume of $\text{Co}_3\text{O}_4/\text{SiO}_2$ are higher when compared with the corresponding bare support, which is unclear at this stage. Nonetheless, the general decrease in the surface area and pore volume observed after catalyst preparation possibly suggests that the Co_3O_4 nanoparticles are mostly located in the pores of each support [41,42].

The concentration of Co (existing as Co_3O_4) in each catalyst was determined using ICP-OES, and the results are summarised in Table 1. The targeted loading of Co_3O_4 was 10 wt.-% (equivalent to 7.3 wt.-% Co). The loading in each catalyst is close to the targeted 10 wt.-% and is also in good agreement with the relative Co_3O_4 weight fractions calculated from PXRD data. Furthermore, the relative decrease in the surface area and pore volume observed after catalyst preparation is proportional to the Co_3O_4 loading calculated using ICP-OES.

Table 1: Summary of the *ex situ* characterisation results for the bare and Co₃O₄-loaded supports.

Sample name	d_{PXRD} (nm)*	$d_{\text{STEM,v}}$ (nm) [§]	$d_{\text{STEM,n}}$ (nm) [#]	SA (m ² /g) [‡]	V_{pore} (cm ³ /g) [‡]	Relative fraction of Co ₃ O ₄ (wt.-%)*	Co ₃ O ₄ loading (wt.-%) [⊥]
Co ₃ O ₄ /CeO ₂	7.7 ± 0.2	16.3 ± 3.7	13.3 ± 3.8	47.5 (53.2)	0.13 (0.18)	6.5 ± 0.8	9.0
Co ₃ O ₄ /ZrO ₂	15.2 ± 0.4	19.1 ± 3.8	16.3 ± 4.1	29.3 (23.1)	0.11 (0.20)	9.8 ± 0.6	9.4
Co ₃ O ₄ /SiC	13.8 ± 0.3	16.9 ± 4.5	12.9 ± 4.3	25.0 (27.9)	0.13 (0.16)	11.3 ± 0.4	9.8
Co ₃ O ₄ /SiO ₂	13.3 ± 0.3	12.0 ± 2.8	9.9 ± 2.7	135.8 (149.0)	0.50 (0.41)	n/a**	9.5
Co ₃ O ₄ /Al ₂ O ₃	13.0 ± 0.2	16.5 ± 3.5	13.9 ± 3.5	136.4 (151.0)	0.40 (0.49)	10.3 ± 0.3	9.5

* volume-based average crystallite size and relative fraction (with associated errors) of Co₃O₄ obtained from Rietveld refinement using TOPAS 5.0.

[§] STEM volume-based average particle size and standard deviation calculated using Equations S15 and S17, respectively.

[#] STEM number-based average particle size and standard deviation calculated using Equations S16 and S18, respectively.

[‡] mass-specific surface area and pore volume from N₂ physisorption. In parentheses is the surface area and pore volume of the corresponding bare support.

[⊥] Co₃O₄ loading calculated from the Co concentration determined using ICP-OES.

** could not be calculated since SiO₂ is amorphous.

3.2. Reduction studies

3.2.1. *In situ* PXRD-based reduction under H₂

The prepared catalysts were reduced in 50% H₂ (with a balance of N₂) at atmospheric pressure by increasing the temperature from 50 to 450 °C to study the effect each support has on the reducibility of Co₃O₄. The phase changes of Co₃O₄ were monitored *in situ* using PXRD. As previously shown, the expected reflections from Co₃O₄ were hardly visible in the *ex situ* PXRD pattern of Co₃O₄/CeO₂ (Figure S4(b)). Similarly, the *in situ* diffraction patterns recorded during the reduction of this catalyst (Figure S9) show no reflections from any Co-based phase. Therefore, for Co₃O₄/CeO₂, only conventional H₂-TPR could inform on the reduction behaviour, and these results are discussed in section 3.2.2.

The *in situ* PXRD patterns recorded for the other supported catalysts are shown in Figures 1 and 2, together with the relative weight fractions and average crystallite sizes of each detected Co-based phase during the reduction between 50 and 450 °C. In reporting the relative fraction of the Co-based phases, the weight fraction of the support was ignored. The crystallite sizes of Co₃O₄ calculated using Rietveld refinement from the *in situ* patterns (Figures 1(c) and 2(c)) are generally higher than those obtained from the *ex situ* patterns (Table 1). This can be attributed to the different measurement parameters chosen, such as the 1/d scan range (*ex situ*: 0.19 – 0.97 Å⁻¹, *in situ*: 0.37 – 0.73 Å⁻¹), the step size (*ex situ*: 4.2 × 10⁻⁴ Å⁻¹, *in situ*: 4.7 × 10⁻⁴ Å⁻¹) and the time per step (*ex situ*: 0.75 seconds, *in situ*: 0.20 seconds), which collectively determine the duration of each scan (*ex situ*: 29 minutes and 50 seconds, *in situ*: 4 minutes and 2 seconds).

In contrast with the unsupported Co₃O₄ catalyst reported in our previous work [9], which reduced to hcp and fcc metallic Co, the Co₃O₄ nanoparticles over the current support materials are ultimately reduced to fcc Co only (Figures 1, 2, S10 and S11). The Al₂O₃-supported catalyst mostly exhibits CoO reflections between 235 and 450 °C, but the intensity of these reflections decreases above 365 °C (Figure 2((a), *right*)). Furthermore, there is a slight broadening of the Al₂O₃ reflection at 1/d = 0.51 Å⁻¹ above 365 °C, which may be caused by the appearance of the main fcc Co reflection at 1/d = 0.49 Å⁻¹. Although no reflections from Co-based phases were observed in the *in situ* PXRD patterns of Co₃O₄/CeO₂ (Figure S9), it is possible that the reduction of the Co₃O₄ only forms fcc Co as well.

Some literature reports have shown the formation of the un-/supported metallic phase as either hcp and fcc Co (*i.e.*, both allotropes co-existing), or only as fcc Co during H₂ reduction. However, this seems to be independent of supporting and independent of the support material used [17,44,45]. On the other hand, metallic Co is thermodynamically more stable in the fcc crystal form below 20 nm, and more stable in the hcp form above 20 nm [46,47]. Therefore, it is possible that the starting particle/crystallite size distribution of Co₃O₄ in the present study (which shows Co₃O₄ particles that are mostly smaller than 20 nm – see Figure S8) results in the formation of metallic crystallites that are below 20 nm (see Figures 1(c) and 2(c)), thus determining the final crystallographic phase of the metal. Moreover, the presence of fcc Co crystallites that are smaller than the starting Co₃O₄ crystallites (Figures 1(c) and 2(c)) indicates that minimal (or no) sintering took place, unlike when unsupported Co₃O₄ was reduced in our previous study [9].

The onset formation of CoO and fcc Co, respectively, in the supported catalysts is observed at temperatures (mostly above 200 °C (*vide infra*)) higher than those observed with our previous unsupported catalyst (which were below 200 °C) [9]. This suggests that supporting Co₃O₄ nanoparticles (achieved *via* incipient wetness impregnation) helps to stabilise the oxide phase during reduction [4,13–15,17,18]. More specifically, this stabilisation could be induced through electronic interactions between the nanoparticles and the support, which may be hindering the diffusion of oxygen species in the supported nanoparticles and/or slowing down H₂ adsorption/dissociation, especially near the nanoparticle-support interface [48,49]. Since the location of (most of) the nanoparticles is inside the pores of each support, this could also delay the onset and/or decrease the extent of reduction as access to the surface adsorption sites of the nanoparticles (to initiate reduction) would be limited [41,42].

The phases CoO and fcc Co first appear at much lower temperatures over SiC (185 and 230 °C), followed by SiO₂ (200 and 265 °C) and then by ZrO₂ (200 and 275 °C) – see Figures 1 and 2. The formation of CoO over Al₂O₃ is observed at 235 °C, and fcc Co is possibly formed at 365 °C, which is inferred from the decreasing intensity of the CoO reflections and the broadening of the Al₂O₃ reflection at $1/d = 0.51 \text{ \AA}^{-1}$ (Figure 2((a), *right*)), as mentioned earlier. Moreover, Co₃O₄ is fully reduced to metallic Co over SiC and ZrO₂ below 325 °C, which may suggest the presence of oxide particles that are weakly interacting with these two supports as also reported in the literature [15,26]. Despite the low onset formation temperature of metallic Co over SiO₂, there seems to be evidence of CoO up to 450 °C given by the continued faint appearance of the main CoO reflection at $1/d = 0.46 \text{ \AA}^{-1}$ (Figure 2((a), *left*)). However, due to

the very low intensity of this CoO reflection above 345 °C, CoO could not be reliably quantified using Rietveld refinement. Nonetheless, the continued presence of CoO might suggest the presence of a small amount of oxide particles/species strongly interacting with the SiO₂ support [4,13,14]. These CoO particles could also be existing as small crystallites, which limits their detection in PXRD, as well as make them harder to reduce (especially in the presence of a support) [6,50,51]. There are slight differences in the starting Co₃O₄ sizes among the supported catalysts (as confirmed with PXRD and STEM-EELS), which can also influence the onset and degree of reduction, with larger crystallites (as those in Co₃O₄/ZrO₂ – see Figures S7 and S8, as well as Table 1) being easier to reduce.

Over the Al₂O₃ support, there remains a significant amount of CoO (45.9 ± 5.0 wt.-%) at 450 °C, together with fcc Co (54.1 ± 6.0 wt.-%). This low reducibility of Co₃O₄/Al₂O₃ is generally reported when the catalyst is prepared *via* (incipient) wetness impregnation [4,14,15,17,18]. The presence of strongly interacting oxide nanoparticles is possible, but also some of the Coⁿ⁺ species could have migrated into the Al₂O₃ lattice, forming Co_xAl_yO_z species during reduction. The formation of bulk cobalt aluminate (CoAl₂O₄) in a H₂ environment directly from Co₃O₄ and CoO, respectively, has been predicted (from thermodynamic calculations) to be more favourable when compared with the formation of Co₂SiO₄ (see Figures S12 and S13).

The known Co-Al and Co-Si oxide phases (*i.e.*, CoAl₂O₄ and Co₂SiO₄) have reflections that would overlap with those from the Al₂O₃ support and/or Co₃O₄ (see Figure S3(d)). The overlap would make it difficult to confirm the presence of these mixed metal oxides using PXRD. However, it is also possible that these phases formed in amounts and/or crystallite sizes that are below the intrinsic detection limits of the current PXRD instrument (*i.e.*, lower than 2 – 3 wt.-% and/or smaller than 2 – 3 nm), or may have formed as amorphous species. The other possibility could be that these species did not form entirely as some researchers have reported temperatures that are above 450 °C for the formation of cobalt aluminate- and cobalt silicate-like species during H₂ reduction [52,53].

According to Equation 2, the final size of CoO is expected to be 96% of the starting size of Co₃O₄ (assuming spherically shaped crystallites and no sintering), however, the average CoO crystallite sizes in Figures 1(c) and 2(c) are significantly smaller than expected. Since the size of the CoO particles could not be determined *in situ* using microscopy, it may be possible that these particles are larger in size but are made up of smaller crystalline domains that are measured using PXRD [43]. The metallic Co is expected to be approximately 80% of the initial

size of Co_3O_4 (see Equation 3) and approximately 83% of the initial size of CoO (see Equation 4). The calculated average metallic Co sizes are also smaller than expected (relative to the starting Co_3O_4 crystallites), but are similar in size to the previously formed CoO crystallites in all catalysts (Figures 1(c) and 2(c)). This observation may imply some degree of crystallite growth during the transformation from CoO to metallic Co as the size of the metal crystallites is higher than the expected 83% crystallite size of CoO. Nonetheless, as mentioned earlier, the final size of the fcc Co in all catalysts is smaller than the initial size of the Co_3O_4 crystallites, which may be a stabilising effect caused by the presence of the support [12].

$$d_{\text{CoO}} = \sqrt[3]{\frac{3 \cdot \rho_{\text{Co}_3\text{O}_4} \cdot M_{\text{CoO}}}{\rho_{\text{CoO}} \cdot M_{\text{Co}_3\text{O}_4}}} \cdot d_{\text{Co}_3\text{O}_4} \approx \mathbf{0.96} \cdot d_{\text{Co}_3\text{O}_4} \quad (2)$$

$$d_{\text{Co}} = \sqrt[3]{\frac{3 \cdot \rho_{\text{Co}_3\text{O}_4} \cdot M_{\text{Co}}}{\rho_{\text{Co}} \cdot M_{\text{Co}_3\text{O}_4}}} \cdot d_{\text{Co}_3\text{O}_4} \approx \mathbf{0.80} \cdot d_{\text{Co}_3\text{O}_4} \quad (3)$$

$$d_{\text{Co}} = \sqrt[3]{\frac{\rho_{\text{CoO}} \cdot M_{\text{Co}}}{\rho_{\text{Co}} \cdot M_{\text{CoO}}}} \cdot d_{\text{CoO}} \approx \mathbf{0.83} \cdot d_{\text{CoO}} \quad (4)$$

$d_{\text{Co}_3\text{O}_4}$, d_{CoO} and d_{Co} are the crystallite sizes of Co_3O_4 , CoO and metallic Co, respectively, assuming spherical shapes. $\rho_{\text{Co}_3\text{O}_4}$, ρ_{CoO} and ρ_{Co} are the densities and $M_{\text{Co}_3\text{O}_4}$, M_{CoO} and M_{Co} are the molecular/atomic masses of Co_3O_4 , CoO and metallic Co, respectively.

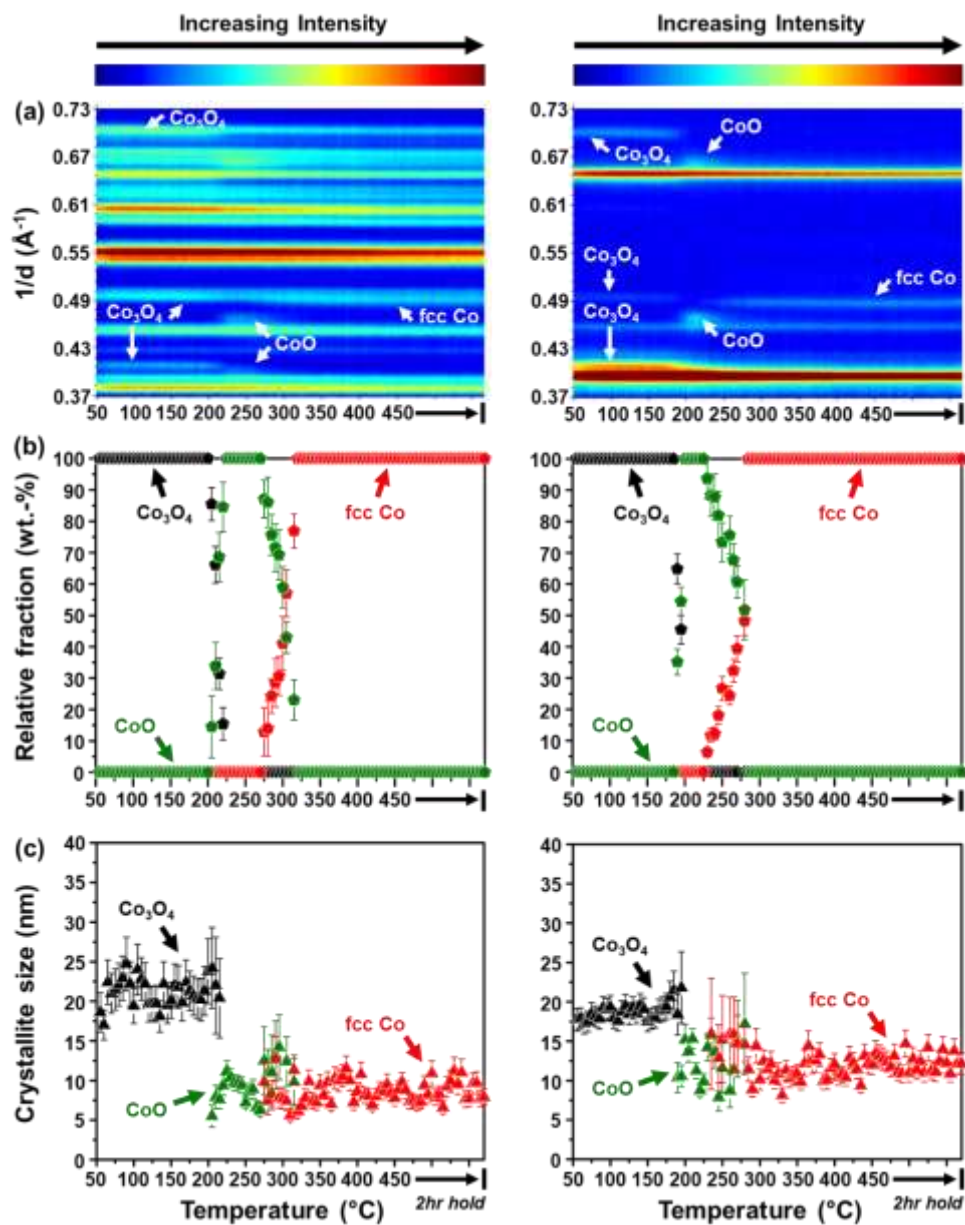


Figure 1: (a) On-top view of the *in situ* PXRD patterns recorded during the reduction of (*left*) $\text{Co}_3\text{O}_4/\text{ZrO}_2$, and (*right*) $\text{Co}_3\text{O}_4/\text{SiC}$ in a mixture of 50% H_2 in N_2 at atmospheric pressure; as well as the (b) relative weight fractions, and (c) average crystallite sizes of the different Co-based phases (excluding the supports) calculated using Rietveld refinement. The white arrows in (a) indicate the reflections from the different Co-based phases present during reduction. These reflections were assigned using the ICDD PDF-2 files of Co_3O_4 , CoO and fcc Co – see Table S4 for the PDF entries.

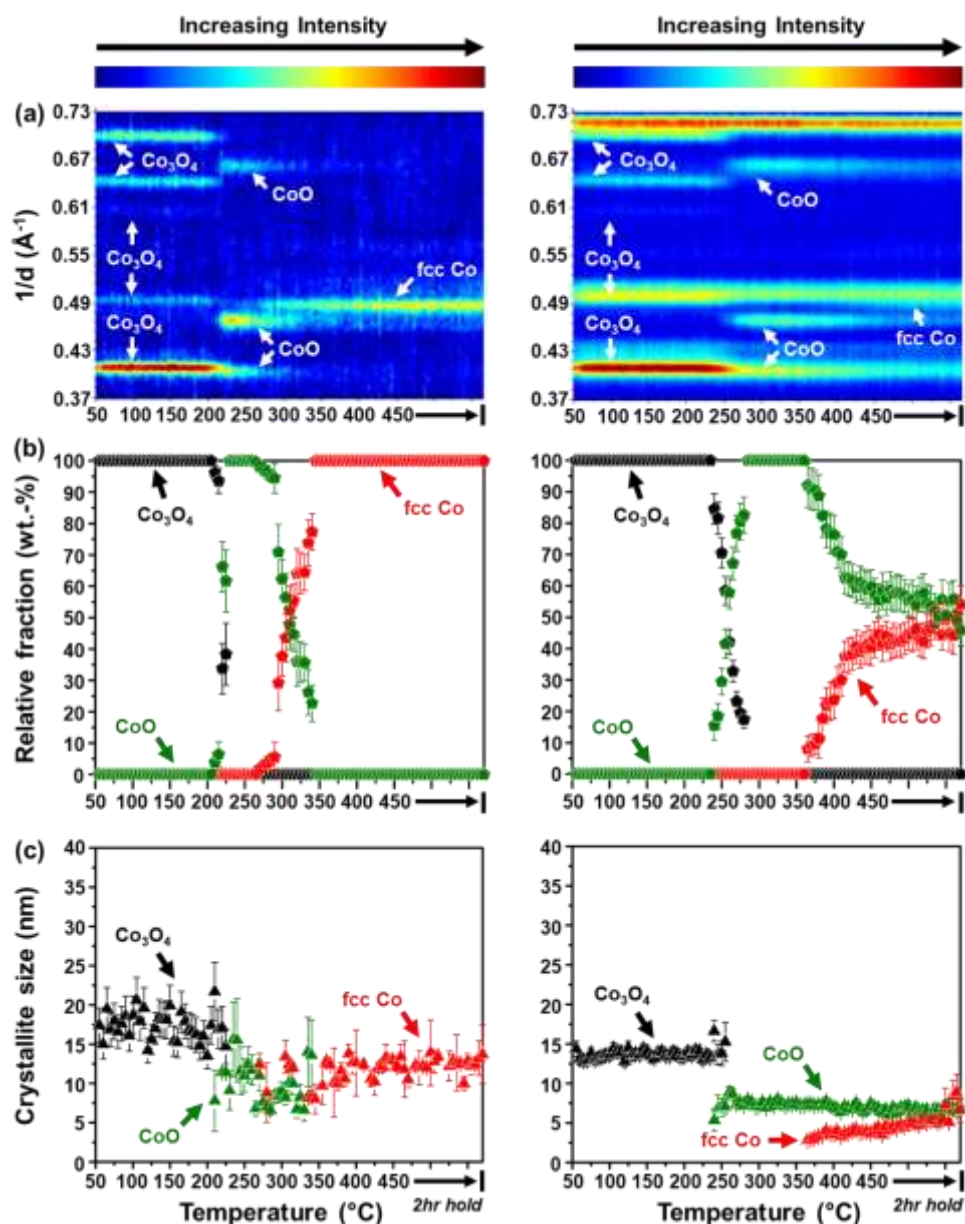


Figure 2: (a) On-top view of the *in situ* PXR D patterns recorded during the reduction of (left) $\text{Co}_3\text{O}_4/\text{SiO}_2$, and (right) $\text{Co}_3\text{O}_4/\text{Al}_2\text{O}_3$ in a mixture of 50% H_2 in N_2 at atmospheric pressure; as well as the (b) relative weight fractions, and (c) average crystallite sizes of the different Co-based phases (excluding the supports) calculated using Rietveld refinement. The white arrows in (a) indicate the reflections from the different Co-based phases present during reduction. These reflections were assigned using the ICDD PDF-2 files of Co_3O_4 , CoO and fcc Co – see Table S4 for the PDF entries.

3.2.2. Conventional H₂-TPR

The reduction of the prepared catalysts was also studied using conventional H₂-TPR in a mixture of 5% H₂ in Ar between 60 and 920 °C. To better understand the reduction profiles of the supported catalysts, the bare supports were also exposed to similar reduction conditions. Noteworthy are the differences in the experimental conditions between the *in situ* PXRD-based reduction and conventional H₂-TPR, such as the concentration of H₂ (50 versus 5%) and heating rate (1 versus 10 °C/min). This can cause differences in the onset temperature (or temperature window) of certain reduction steps as detected by the two instruments. However, the trends in the reducibility of the different supported catalysts are still analogous between the techniques.

The bare ZrO₂, SiC, SiO₂ and Al₂O₃ supports do not undergo reduction within the temperature window studied (Figure 3(a)). However, for the bare CeO₂ support, two reduction peaks are observed – the first is between 320 and 570 °C, and the other is between 570 and 920 °C. The low temperature peak is normally assigned to the reduction of (sub-)surface CeO₂ species, and the high temperature peak is assigned to the reduction of the bulk species to form Ce₂O₃ [54–56]. From the reduction profile of the bare CeO₂, the estimated DoR to Ce₂O₃ is 55.6% (see Table 2), which indicates that CeO₂ is only partially reduced between 60 and 920 °C. The reduction profiles of the Co₃O₄-loaded supports exhibit reduction peaks that are not observed in the profiles of the bare supports (Figure 3(b)), implying that the supported Co₃O₄ nanoparticles are the ones (mostly) undergoing reduction.

The reduction profile of the Co₃O₄/CeO₂ catalyst (Figure 3(b)) shows three peak maxima below 530 °C and one at 725 °C. The profile of the bare CeO₂ support also has a peak maximum at 725 °C, implying that the reduction taking place in both samples at this high temperature is of the bulk CeO₂ species [54–56]. Therefore, the peaks below 530 °C in the profile of Co₃O₄/CeO₂ can be attributed to the reduction of Co-based species. The first two low temperature peaks may be for the formation of CoO and metallic Co, respectively, originating from Co₃O₄ that is weakly interacting with the CeO₂ [55,56]. The third peak at 450 °C could be for the Co species strongly interacting with the CeO₂, possibly near the nanoparticle-support interface. This third reduction peak is at a lower temperature (450 °C) when compared with the first reduction peak of the bare CeO₂ support (490 °C – see Figure 3(a)), which was assigned to the reduction of (sub-)surface CeO₂. Therefore, it is possible that in the presence of reduced Co, the (sub-

)surface CeO_2 reduces at a lower temperature of $450\text{ }^\circ\text{C}$ due to H_2 spillover from reduced Co [55,56]. It is possible that part of this low temperature reduction of (sub-)surface CeO_2 also took place during the PXRD-based reduction (performed between 50 and $450\text{ }^\circ\text{C}$ – see Figure S9), but was not observed as PXRD is not a surface-sensitive technique and has relatively high detection limits as mentioned earlier.

The DoR of $\text{Co}_3\text{O}_4/\text{CeO}_2$ (which is 94.3% – see Table 2) was calculated between 150 and $530\text{ }^\circ\text{C}$ as this is the temperature window where (most of) the Co species are assumed to have reduced. It remains possible that some Co species also reduced at higher temperatures but this may have been concurrent with the partial reduction of the bulk CeO_2 species. Furthermore, it has been proposed in literature that Co and Ce could form an irreducible mixed metal oxide during reduction [55,56], which can be facilitated by the migration of partially reduced ceria species to the partially reduced cobalt species [57].

In the reduction profile of $\text{Co}_3\text{O}_4/\text{ZrO}_2$, multiple reduction peaks are observed between 150 and $450\text{ }^\circ\text{C}$ (Figure 3(b)), which may be a result of having particles/crystallites of different sizes reducing at different temperatures [6,50,51]. This is in addition to the two-step transformation of Co_3O_4 to CoO and then to metallic Co, which is also size- and temperature-dependent. The ZrO_2 -supported catalyst does not exhibit significant reduction above $450\text{ }^\circ\text{C}$ (despite the estimated DoR of 95.5%), unlike the other supported catalysts. Therefore, it is possible that the DoR of 95.5% is a result of a slight underestimation of the H_2 consumption by the instrument or an underestimation of the reduction peak areas. The complete reduction of $\text{Co}_3\text{O}_4/\text{ZrO}_2$ was also confirmed using *in situ* PXRD at $450\text{ }^\circ\text{C}$, despite the differences in the onset temperatures for the transformation of the different Co-based phases observed using the two reduction techniques.

Over SiC , SiO_2 and Al_2O_3 , there are two reduction peaks observed between 190 and $450\text{ }^\circ\text{C}$, which can be assigned to the two-step reduction of weakly interacting Co_3O_4 particles transforming into CoO and then to metallic Co [4,8,13,14,16]. Above $450\text{ }^\circ\text{C}$, the SiC - and SiO_2 -supported catalysts display some slight reduction up to 620 and $740\text{ }^\circ\text{C}$, respectively, possibly indicating the presence of small amounts of Co species strongly interacting with these two supports. The evidence of these strongly interacting Co species was observed during the PXRD-based reduction of $\text{Co}_3\text{O}_4/\text{SiO}_2$ (Figure 2((a), *left*)) but not observed for $\text{Co}_3\text{O}_4/\text{SiC}$ (Figure 1((a), *right*)); possibly due to their amorphous nature, very low concentration and/or small crystallite size. We further propose that the species reducing at temperatures above 450

°C over SiC could be located at the nanoparticle-support interface, as the surface of SiC has a 1 – 2 nm Si_xO_y or $\text{Si}_x\text{O}_y\text{O}_z$ layer (see Figure S14(b) for the STEM-EELS micrographs) which is formed during the commercial synthesis of the support [26].

In the Al_2O_3 -supported catalyst, there are Co species that reduce between 450 and 740 °C, with the other species reducing between 740 and 920 °C. These high temperature reduction peaks are normally associated with the reduction of strongly interacting Co oxide species and/or Co-Al oxide species in the form of $\text{Co}_x\text{Al}_y\text{O}_z$ [4,8,14,16,18]. The $\text{Co}_x\text{Al}_y\text{O}_z$ species may have been present in the fresh calcined catalyst or may have formed during the reduction due to the migration of Co^{nt} species into the Al_2O_3 lattice. Furthermore, the reduction of Co species at very high temperatures is also in agreement with the PXRD-based reduction results which showed a partial reduction of CoO to metallic Co at 450 °C (Figure 2, *right*). Nonetheless, the DoR of Co_3O_4 to metallic Co over SiC, SiO_2 and Al_2O_3 reaches values above 90% at 920 °C, with SiC reaching the highest value of 98.3% (Table 2).

As can be seen in Table 2, the DoR of Co_3O_4 to metallic Co over the various supports follows the trend: SiC (98.3%) > ZrO_2 (95.5%) > CeO_2 (94.3%) > SiO_2 (91.0%) > Al_2O_3 (90.2%). This trend is in agreement with the overall trend observed during the PXRD-based reduction experiments, where Co_3O_4 was fully reduced over SiC and ZrO_2 below 325 °C, while over SiO_2 and Al_2O_3 , reflections from CoO could still be observed at the highest temperature of 450 °C.

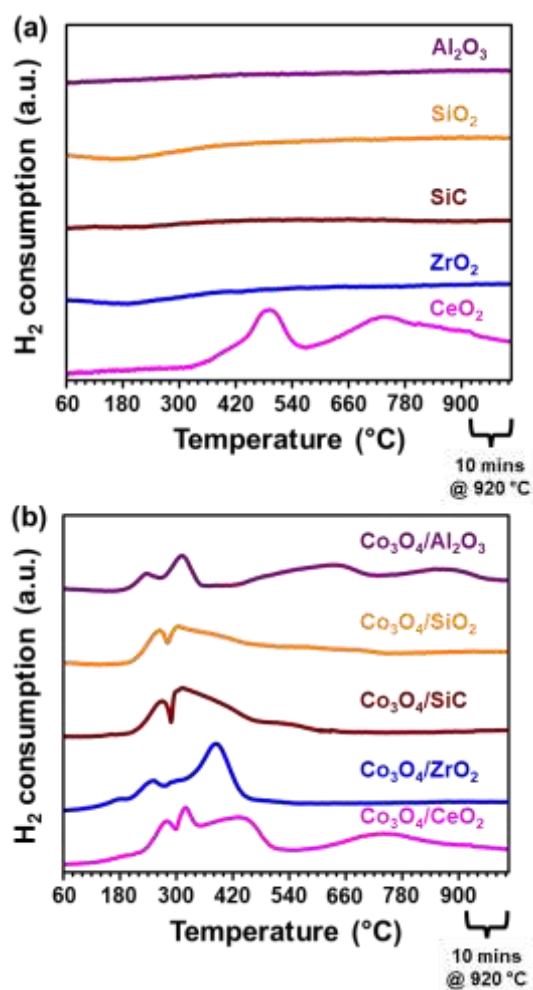


Figure 3: Reduction profiles of the (a) bare, and (b) Co_3O_4 -loaded supports derived from conventional H_2 -TPR in a mixture of 5% H_2 in Ar at atmospheric pressure. The y-axis range in (a) is a factor of 2 shorter than the y-axis in (b).

Table 2: Degree of reduction (DoR) of each supported catalyst after H_2 -TPR. The DoR of bare CeO_2 is also included.

Sample name	DoR (%)
CeO_2	55.6
$\text{Co}_3\text{O}_4/\text{CeO}_2$	94.3*
$\text{Co}_3\text{O}_4/\text{ZrO}_2$	95.5
$\text{Co}_3\text{O}_4/\text{SiC}$	98.3
$\text{Co}_3\text{O}_4/\text{SiO}_2$	91.0
$\text{Co}_3\text{O}_4/\text{Al}_2\text{O}_3$	90.2

* DoR is for the Co-based species assumed to have reduced between 150 and 530 °C.

3.3. *In situ* catalyst characterisation and evaluation

3.3.1. Effect of different supports in dry CO-PrOx

All supported catalysts were evaluated under dry CO-PrOx conditions and characterised *in situ* using PXRD [27–29] and magnetometry [29,30]. The gas feed contained 1% CO, 1% O₂, 50% H₂ and 48% N₂ being flowed at a GHSV of 60000 mL(NTP)/g_{Co₃O₄}/hr at atmospheric pressure, while varying the temperature stepwise between 50 and 450 °C. Figures 4 – 6 show the PXRD-derived relative weight fractions and average crystallite sizes of the detected Co-based phases, the normalised outlet gas flow rates, and the magnetometry-derived DoR of Co₃O₄ to metallic Co as a function of temperature for each catalyst. The recorded *in situ* diffraction patterns are presented in Figure S15, and selected Rietveld refinement results (including the fitted phases) can be found in Figures S16 and S17. Figure 7 shows a comparison of all the tested catalysts in terms of CO conversion and O₂ selectivity to CO₂, respectively, CO conversion to CH₄, and the magnetometry-derived DoR. The changes in the CO conversion and O₂ selectivity to CO₂ between 50 and 200 °C – where the Co₃O₄ phase appears to be stable in all the prepared catalysts – are replotted in Figure S18. Water formation could not be measured as the water was condensed before allowing the other gases in the reactor effluent to enter the micro-GC. However, the formation of water was inferred *via* an oxygen balance. PXRD measurements for Co₃O₄/CeO₂ were not carried out during dry CO-PrOx as previously discussed *ex situ* (Figure S4(b)) and *in situ* (Figure S9) results show the difficulty in detecting Co-based phases in the presence of the CeO₂ support.

A comparison of all the prepared catalysts between 50 and 200 °C, where the Co₃O₄ phase is still stable, reveals the following trend in terms of the highest CO conversion to CO₂ achieved: ZrO₂ (91.5%) > SiC (80.8%) > SiO₂ (66.9%) > CeO₂ (55.8%) > Al₂O₃ (26.6%) – see Figures 4 – 7, and S18(a). These highest CO conversions are all observed at 200 °C. The CO conversion of 91.5% attained over Co₃O₄/ZrO₂ at 200 °C is still lower than the targeted 99.999% CO conversion in the context of H₂ purification for PEMFCs [10,11]. Nonetheless, the ZrO₂-supported catalyst also showed superior performance when compared with our previously reported unsupported Co₃O₄ catalyst [9], which attained a 84.4% CO conversion to CO₂ at 200 °C under the same reaction condition. Since equal amounts of CO and O₂ were present in the feed, it is expected that the conversion of O₂ will be half of the conversion of CO, assuming

that O₂ is only consumed *via* CO oxidation (also see Equation 5). However, the normalised outlet flow rate of O₂ over all catalysts decreases to zero at elevated reaction temperatures (Figures 4 – 6), which indicates the undesired concurrent conversion of H₂ to H₂O (see Equation 6). Further evidence of this is shown in Figures 7(b) and S18(b) where the O₂ selectivity to CO₂ is below 100% at all temperatures, and shows a continuous decrease above 150 °C. At low normalised outlet flow rates of O₂ (*i.e.*, high O₂ conversions), the Co₃O₄ phase in each catalyst reduces to unwanted CoO, which is less active and selective [5–9,58], as also evidenced by the decreasing CO conversion and O₂ selectivity to CO₂ with temperature over this new phase.



The CoO over ZrO₂, SiC and SiO₂ is observed from 225 °C, while over Al₂O₃, CoO is only observed from 275 °C (Figures 5(a), 6(a) and S15). Despite the different conditions applied, there is an agreement between the results from the reduction experiments (PXRD-based and conventional TPR) and the dry CO-PrOx experiments in terms of the reducibility of Co₃O₄ to CoO, where this is easier over ZrO₂, SiC and SiO₂, and harder over Al₂O₃. This can be attributed to the nature/strength of the NPSI, which may be affecting the rate of diffusion of oxygen species in cobalt oxide and/or the rate of H₂ adsorption/dissociation as proposed earlier [48,49]. The differences in the starting Co₃O₄ sizes between the supported catalysts can also influence the onset of reduction [6,50,51]. The formation of CoO in all supported catalysts takes place at higher temperatures when compared with our previous unsupported Co₃O₄ catalyst, where this took place at 200 °C [9]. As mentioned earlier, the expected crystallite size of CoO is 96% of the starting size of Co₃O₄ (assuming spherical crystallites and no sintering – see Equation 2). Figures 5(b) and 6(b) show that the calculated average size of the CoO crystallites formed over all supports is smaller than the expected size, which indicates minimal (or no) sintering. However, it is possible that larger particles of CoO were formed which are made up of smaller crystalline domains that are measured using PXRD [43].

Assuming that the Co₃O₄ phase is more active than CoO for CO oxidation [5–9,58], and that this reaction takes place *via* the MvK mechanism over Co₃O₄ [1,19–21], the observed trends

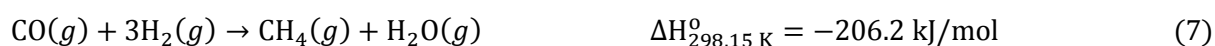
for the Co_3O_4 -to- CoO transformation could be related to the CO oxidation activity. For example, Co_3O_4 reduces (on the surface and bulk) relatively easier over ZrO_2 , and this may be the reason for its high CO oxidation activity as the MvK mechanism becomes more facile over Co_3O_4 , before reaching very low gas phase O_2 concentrations. Similar to $\text{Co}_3\text{O}_4/\text{ZrO}_2$, the SiC- and SiO_2 -supported catalysts exhibit Co_3O_4 reduction to CoO from 225 °C, but show lower CO oxidation activity than the ZrO_2 -supported catalyst, possibly indicating a less facile MvK mechanism in these two catalysts. The very low CO oxidation activity of the Al_2O_3 -supported catalyst could also be explained by the observed high onset reduction temperature (275 °C), which possibly points towards a low surface reducibility and consequently, an even less effective MvK mechanism.

The $\text{Co}_3\text{O}_4/\text{CeO}_2$ catalyst is also less active when compared with the ZrO_2 -, SiC- and SiO_2 -supported catalysts, which was unexpected as both CeO_2 and Co_3O_4 are reducible oxides, with CeO_2 also known to promote CO oxidation activity through the provision of oxygen species at the nanoparticle-support interface [59,60]. It may be possible that other effects negatively influence the activity of $\text{Co}_3\text{O}_4/\text{CeO}_2$, such as particle size (see size distribution in Figure S8 derived from STEM-EELS), which is known to have an impact on CO oxidation [1,3,6]. There also exist some clustered Co_3O_4 particles in the fresh catalyst, which may have limited the ideal interaction between Co_3O_4 and CeO_2 to maximise the promotional effect of the support. However, we are unable to provide further details on the above-mentioned possible effects at this stage.

A further increase in the reaction temperature transforms CoO to metallic Co , as confirmed using PXRD and magnetometry, which results in the undesired formation of CH_4 from CO and H_2 (Equation 7) over all evaluated catalysts (Figures 4 – 7). Similar to the PXRD-based reduction experiments (Figures 1 and 2), only metallic fcc Co is formed during dry CO-PrOx. Based on the magnetometry results, $\text{Co}_3\text{O}_4/\text{CeO}_2$ and $\text{Co}_3\text{O}_4/\text{ZrO}_2$ form metallic Co at 250 °C, while $\text{Co}_3\text{O}_4/\text{SiC}$ and $\text{Co}_3\text{O}_4/\text{SiO}_2$ form the metallic phase at 275 °C, and $\text{Co}_3\text{O}_4/\text{Al}_2\text{O}_3$ at 325 °C. Methane formation is first observed at very similar temperatures as the above-mentioned onset formation temperatures for metallic Co . However, over $\text{Co}_3\text{O}_4/\text{Al}_2\text{O}_3$, CH_4 is formed at a higher temperature (375 °C) than the metallic Co formation temperature (325 °C). This might be due to a kinetically hindered CO and/or H_2 dissociation over the metallic phase below 375 °C [61,62]. The low H_2 dissociation activity (or low hydrogen surface coverage) could also explain the delayed reduction of Co_3O_4 and CoO over Al_2O_3 , when compared with the other support materials.

The magnetometry-derived onset formation temperatures for metallic Co are lower than those observed during the complementary PXRD study. Furthermore, the metallic phase is not observed in the acquired PXRD patterns for the Co₃O₄/Al₂O₃ catalyst (Figures S15(d) and S17((c), *right*)). These observations may be explained by the previously mentioned higher intrinsic detection limits of PXRD in terms of crystallite size, phase concentration and crystallinity, which only allowed for fcc Co to be detected at higher temperatures. The trend in the final magnetometry-derived DoR at 450 °C is as follows: ZrO₂ (100%) > CeO₂ (72.4%) > SiC (41.5%) > SiO₂ (22.1%) > Al₂O₃ (16.2%). PXRD analysis also confirmed complete reduction of Co₃O₄ to fcc Co over ZrO₂, but estimated a lower relative amount of the metal over SiC (33.8 ± 9.3 wt.-%) at 450 °C. Surprisingly, the estimated amount of fcc Co over SiO₂ from PXRD (46.1 ± 8.8 wt.-%) is much higher than the magnetometry-derived DoR (22.1%) at 450 °C. The overestimation of fcc Co based on PXRD might be caused by the amorphous background signal from the SiO₂ support, which affects the relative intensity of the reflections from CoO and fcc Co in the acquired patterns.

The PXRD-derived average sizes of the fcc Co crystallites formed over SiC and SiO₂ are similar to the size of the CoO crystallites, which indicates slight crystallite growth during the reduction of CoO to fcc Co (Figure 5(b) and 6(b)), as the expected size of fcc Co is supposed to be 83% of the previously formed CoO (see Equation 4). However, the fcc Co crystallites are still smaller than the starting Co₃O₄ crystallites. On the other hand, the metallic crystallites formed over ZrO₂ are similar in size as the starting Co₃O₄ crystallites, which indicates a higher degree of sintering during the CoO-to-fcc Co reduction, as the size of the metal is expected to be 80% of the size of Co₃O₄ (see Equation 3). This higher degree of sintering may indicate the existence of weaker NPSI in Co₃O₄/ZrO₂ when compared with the other catalysts [12]. Furthermore, the crystallite growth may have been facilitated by the relatively high partial pressures of H₂O formed during dry CO-PrOx [25,63,64], as a result of H₂ oxidation, CO methanation, and catalyst reduction.



It is interesting to note the relatively low DoRs for the SiC- and SiO₂-supported catalysts, which were unexpected in the current study. In reported literature [26], the use of SiC as a support

helps to prevent/limit the development of strong NPSI that may hinder the reduction of the supported metal oxide and/or cause the metal oxide to react with the support to form irreducible mixed metal oxide species. On the other hand, SiO₂ is generally preferred over Al₂O₃ as a catalyst support as it can allow for higher DoRs and is less likely to form mixed metal oxide species during reduction [4,14,18,25] (also see results from thermodynamic calculations in Figures S12 and S13 based on Co₃O₄ and CoO reduction, respectively). There may be other factors contributing to the low reducibility of the SiC- and SiO₂-supported catalysts, especially from CoO to metallic Co (Figures 5 – 7), such as the varying partial pressure ratio of H₂:H₂O at high temperatures, which is caused by the occurrence of H₂ oxidation, CO methanation, and catalyst reduction. Furthermore, the adsorption strengths and/or dissociation rates of the H₂ and H₂O may also be altered as a result of the nature of the CoO-support interaction [48,49]. As previously mentioned, the CoO-SiC interaction may be through the thin Si_xO_y or Si_xO_yC_z layer present around the core SiC particles (see Figure S14(b) for the STEM-EELS micrographs) [26].

Unlike in previous studies [5–8], the increase in the DoR with increasing temperature in the present study does not necessarily result in high CO conversions to CH₄ (as observed with Co₃O₄/CeO₂ above 300 °C – see Figures 4 and 7). Similarly, low degrees of reduction do not always result in low amounts of CH₄ being formed (as observed with Co₃O₄/SiC and Co₃O₄/SiO₂ – see Figures 5 – 7). Methane formation is a surface-specific reaction, while the DoR (based on the characterisation techniques used) is a bulk phenomenon. Therefore, it is possible that the kind and/or number of active sites required for CO methanation were not formed or accessible on the surface of the CeO₂-supported catalyst, resulting in low methanation activity above 300 °C, even though relatively high DoRs were achieved [9,65]. On the other hand, the high methanation activity of the SiC- and SiO₂-supported catalysts, with low DoRs, may be possible through having the required type and/or number of surface active sites.

Particularly interesting is the methanation activity of the CeO₂-supported catalyst, which initially increases between 250 and 300 °C, and then gradually decreases between 300 and 450 °C (Figures 4(a) and 7(c)). Taking place concurrently is the continuous increase in the DoR of this catalyst between 250 and 450 °C (Figures 4(b) and 7(d)). The H₂-TPR profile of the bare CeO₂ support showed a peak maximum at 490 °C, which was assigned to the possible reduction of some (sub-)surface CeO₂ species (see Figure 3(a)) [55,56]. This reduction peak shifted to 450 °C in the presence of reduced Co-based species (originating from the initial Co₃O₄/CeO₂

catalyst – see Figure 3(b)), possibly due to a H₂ spillover effect. Such reduced ceria species could migrate and adsorb on the surface of metallic Co (and over some CoO_{1-x} species), similar to the observations made by Bernal *et al.* [57] (*via ex situ* HRTEM) for Rh, Pd and Pt nanoparticles, respectively, supported on CeO₂. The reduction of (sub-)surface ceria species and their subsequent migration, may have also taken place during dry CO-PrOx. This could lead to the blockage of active sites and consequently decrease methanation activity, as observed between 300 and 450 °C (Figures 4(a) and 7(c)). The formation of Co-Ce oxides during dry CO-PrOx (proposed earlier during H₂-TPR [55,56]) might have also taken place as the Co₃O₄/CeO₂ catalyst reaches a maximum DoR of 72.4% at 450 °C (Figures 4(b) and 7(d)). However, this DoR is still much higher than that reached by the SiC-, SiO₂- and Al₂O₃-supported catalysts, which possibly suggests that the interactions in Co₃O₄/CeO₂ do not significantly hinder the formation of metallic Co.

Although the ultimate formation of metallic Co at elevated temperatures over the different supports decreases the CO oxidation activity and selectivity, the catalysts (except Co₃O₄/ZrO₂) continue to form relatively small amounts of CO₂ over the metallic phase (see Figures 4 – 7). This may be attributed to an *in situ* WGS reaction, which firstly involves H₂O formation from H₂ and O₂ (Equation 6), and then this H₂O subsequently reacts with CO to form CO₂ and H₂ (Equation 8) [7,9].



The work presented in this section shows how different oxidic (CeO₂, ZrO₂, SiO₂ and Al₂O₃) and non-oxidic (SiC) supports can affect the catalytic performance and phase stability of Co₃O₄ nanoparticles during dry CO-PrOx (*i.e.*, in the absence of H₂O and CO₂ co-feeding). More specifically, the influence of each support could be attributed to the nature and/or strength of the NPSI, which can possibly affect the surface reducibility (and re-oxidation potential) of Co₃O₄ required for an effective MvK mechanism for CO oxidation [1,19–21]. The existence of NPSI might also determine the bulk reducibility of Co₃O₄ to CoO and metallic Co at elevated reaction temperatures [4,8,13–16,18,23].

When Co₃O₄ is supported on ZrO₂, high CO conversions to CO₂ are achievable (see Figures 7(a) and S18(a) between 50 and 200 °C), possibly indicating a more facile MvK mechanism

due to the existence of relatively weak NPSI. The Al_2O_3 -supported catalyst achieves the lowest CO conversions to CO_2 , indicating a less effective MvK mechanism due to the presence of strong NPSI. As a result of weak interactions, unwanted metallic Co and CH_4 are formed at relatively low temperatures (especially over $\text{Co}_3\text{O}_4/\text{ZrO}_2$ and $\text{Co}_3\text{O}_4/\text{CeO}_2$), whereas the strong interactions in $\text{Co}_3\text{O}_4/\text{Al}_2\text{O}_3$ may have caused the observed highest increase in the onset formation temperature for metallic Co and CH_4 (see Figures 7(c) and (d)). Therefore, these observations highlight the importance of having a bi-functional support that can help stabilise the Co_3O_4 phase while keeping it active for CO oxidation over a wide temperature range.

Furthermore, since there are Co_3O_4 particles of varying sizes in each fresh catalyst (see size distributions in Figure S8), this could have also played a role in determining the overall CO oxidation activity [1,3,6] and phase stability of Co_3O_4 [6,50,51].

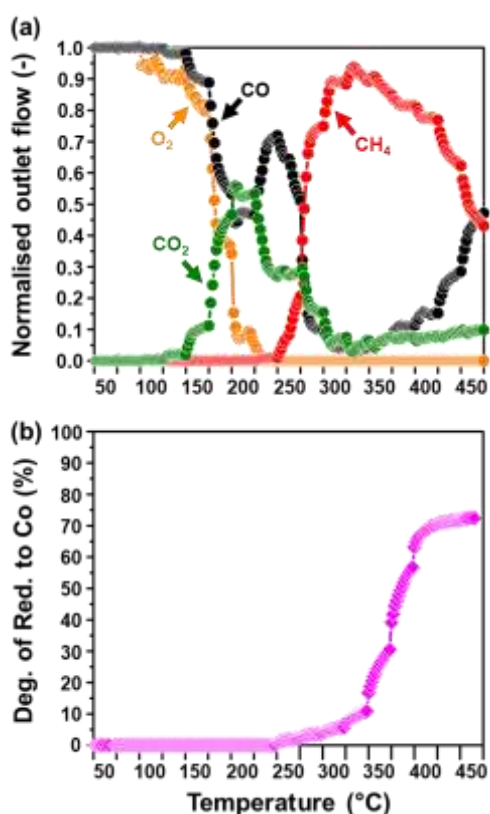


Figure 4: (a) Normalised outlet flow rates of CO , O_2 , CO_2 and CH_4 ; as well as the (b) magnetometry-derived DoR of Co_3O_4 to metallic Co for $\text{Co}_3\text{O}_4/\text{CeO}_2$. (Feed composition: 1% CO , 1% O_2 , 50% H_2 and 48% N_2 ; pressure: atmospheric, GHSV: 60000 $\text{mL(NTP)}/\text{g}_{\text{Co}_3\text{O}_4}/\text{hr}$).

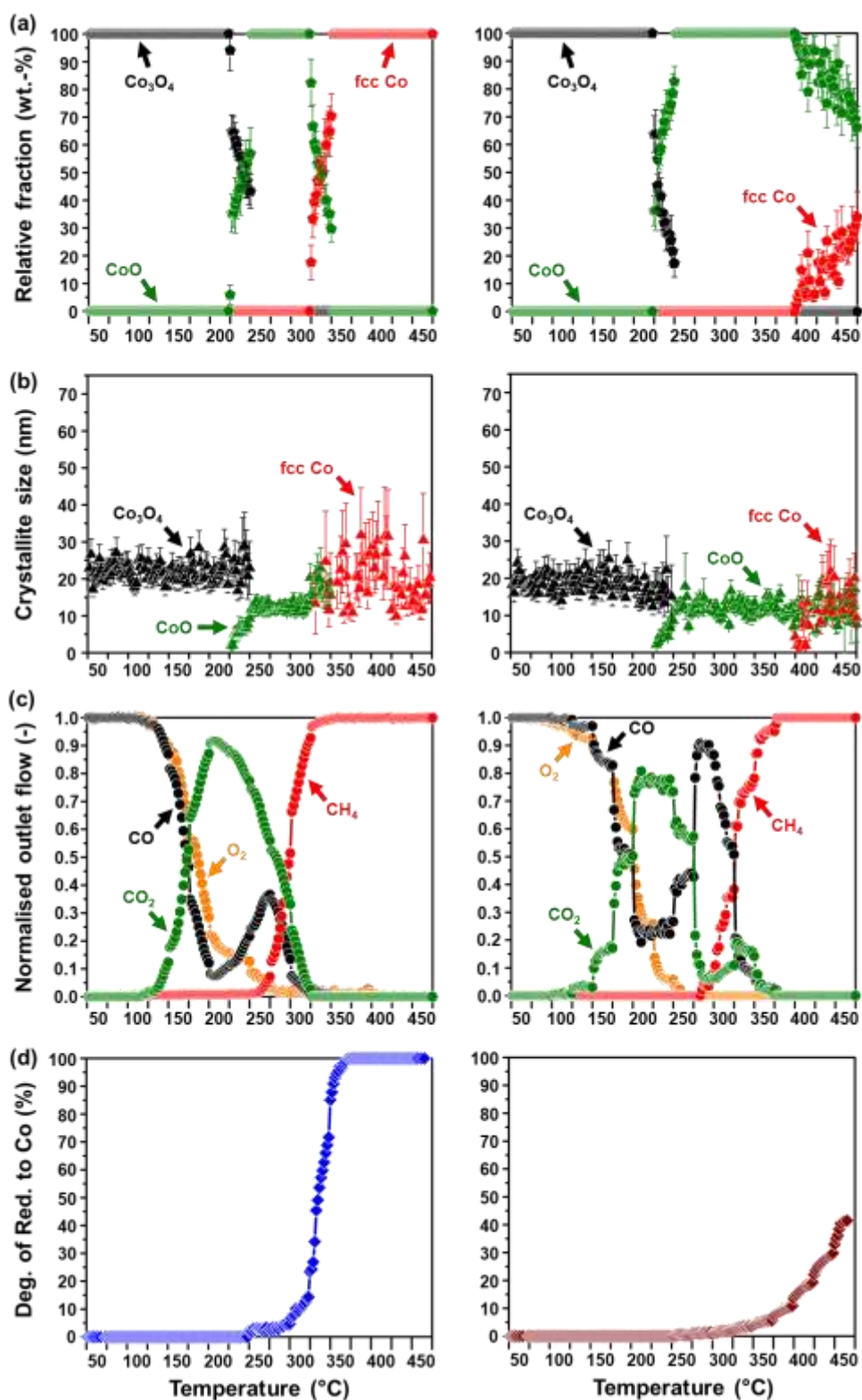


Figure 5: (a) PXRD-derived relative weight fractions, and (b) average crystallite sizes of the different Co-based phases formed (excluding the supports), (c) normalised outlet flow rates of CO, O₂, CO₂ and CH₄; as well as the (d) magnetometry-derived DoR of Co₃O₄ to metallic Co for (left) Co₃O₄/ZrO₂, and (right) Co₃O₄/SiC. (Feed composition: 1% CO, 1% O₂, 50% H₂ and 48% N₂; pressure: atmospheric, GHSV: 60000 mL(NTP)/g_{Co₃O₄}/hr).

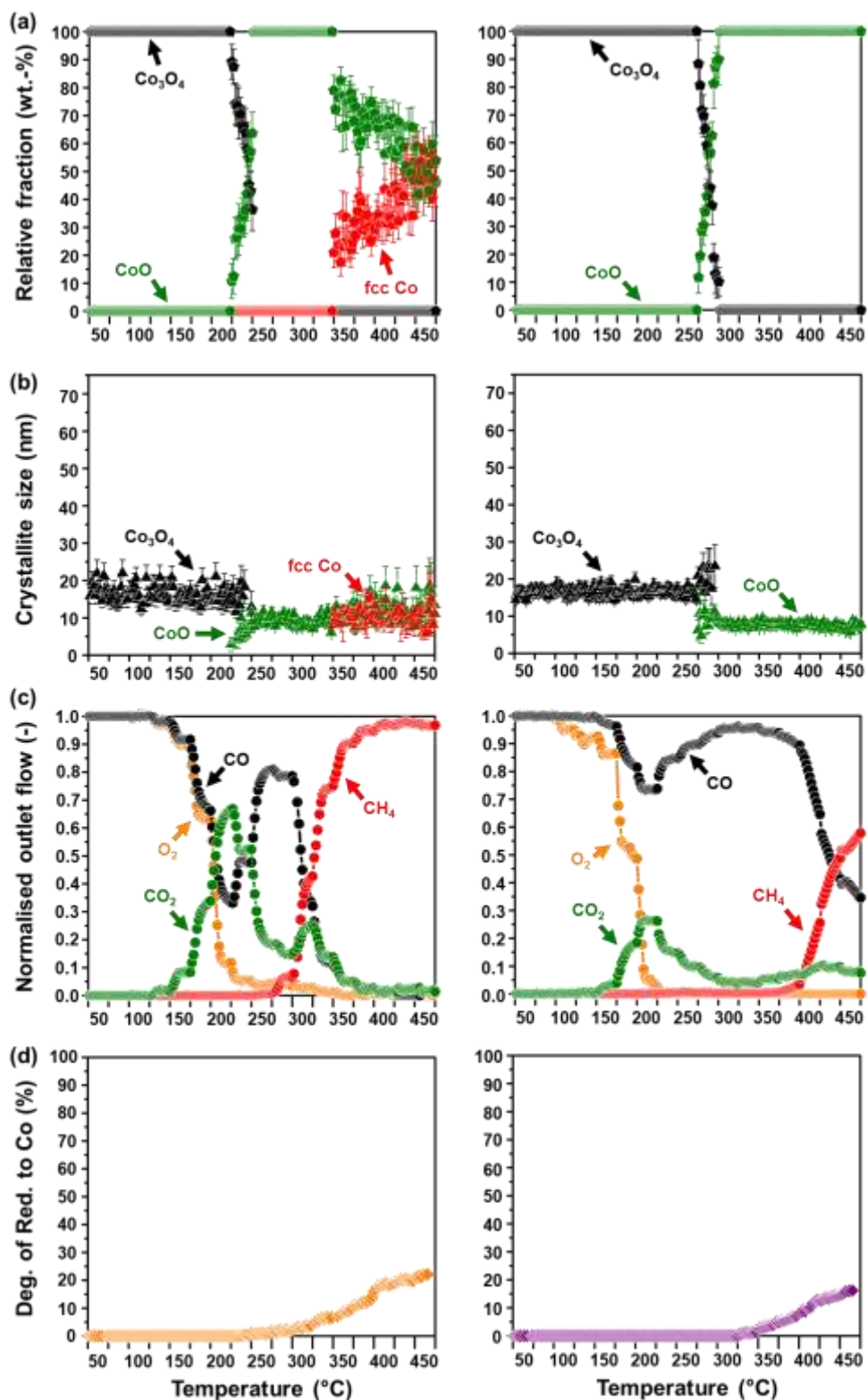


Figure 6: (a) PXRD-derived relative weight fractions, and (b) average crystallite sizes of the different Co-based phases formed (excluding the supports), (c) normalised outlet flow rates of CO, O₂, CO₂ and CH₄; as well as the (d) magnetometry-derived DoR of Co₃O₄ to metallic Co for (*left*) Co₃O₄/SiO₂, and (*right*) Co₃O₄/Al₂O₃. (Feed composition: 1% CO, 1% O₂, 50% H₂ and 48% N₂; pressure: atmospheric, GHSV: 60000 mL(NTP)/g_{Co₃O₄}/hr).

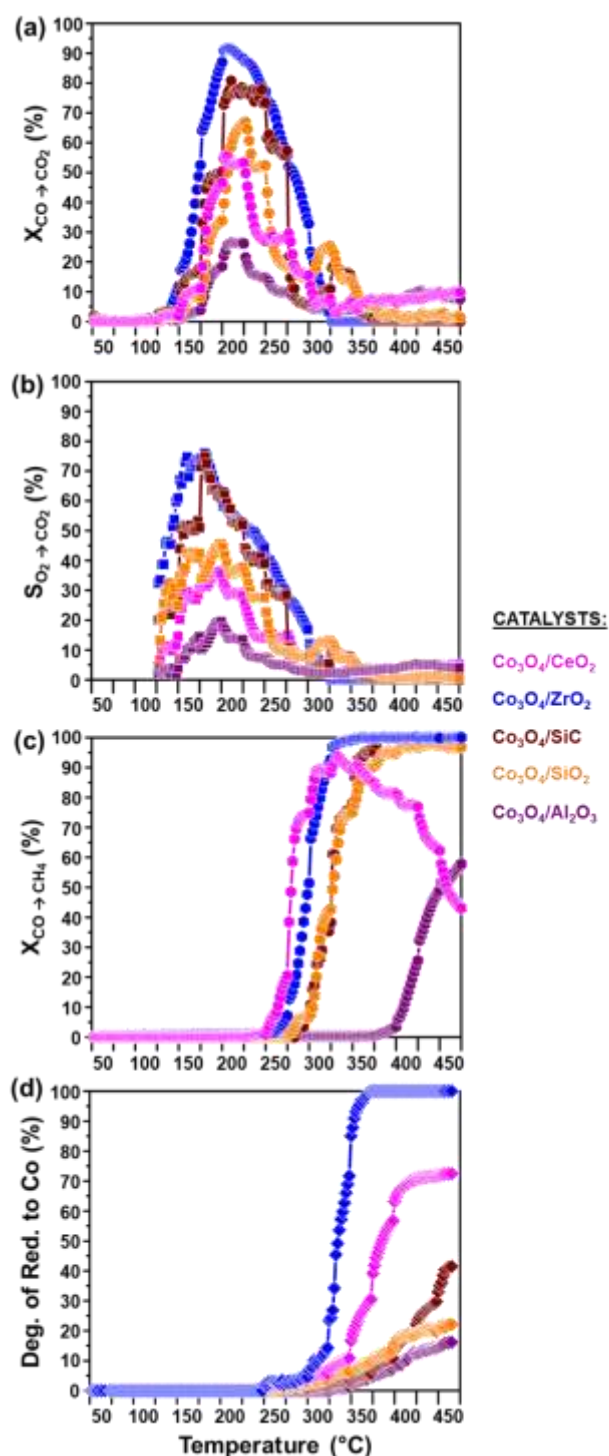


Figure 7: (a) CO conversion to CO₂ ($X_{\text{CO} \rightarrow \text{CO}_2}$), (b) O₂ selectivity to CO₂ ($S_{\text{O}_2 \rightarrow \text{CO}_2}$), (c) CO conversion to CH₄ ($X_{\text{CO} \rightarrow \text{CH}_4}$), and the (d) magnetometry-derived DoR of Co₃O₄ to metallic Co for all prepared catalysts. The O₂ selectivity to CO₂ was calculated at temperatures where both CO and O₂ were converted (see Figures 4(a), 5(c), 6(c) and 7(a)). Also see Figure S18 which shows the changes in the CO conversion and O₂ selectivity to CO₂ between 50 and 200 °C, where the Co₃O₄ phase appears to be stable in all evaluated catalysts based on *in situ* PXRD analysis. (Feed composition: 1% CO, 1% O₂, 50% H₂ and 48% N₂; pressure: atmospheric, GHSV: 60000 mL(NTP)/g_{Co₃O₄}/hr).

3.3.2. Effect of co-fed H₂O and CO₂ in CO-PrOx

The gases H₂O and CO₂ form part of a realistic CO-PrOx feed [10,11]; however, their effect on the CO oxidation activity/selectivity and the phase stability of oxide catalysts has not been studied extensively as that of H₂. These two gases have known oxidising capabilities (with H₂O being stronger than CO₂ [9]) and can be expected to stabilise the oxide phase of the catalyst during the reaction. Moreover, the presence of H₂O can cause the forward WGS reaction (Equation 8) to take place [5,9], while CO₂ can result in CO₂ methanation (Equation 9) and the reverse WGS reaction (Equation 10) [5,9]. The possible occurrence of the above-mentioned individual reactions (as well as CO oxidation, H₂ oxidation and CO methanation) can complicate the analysis of the reactor effluent as one gas can be converted and/or produced from at least two of these reactions [9]. Therefore, we chose to present the results from the analysis of the effluent gas as positive and negative net outlet flow rates of the gases CO, O₂, CO₂ and CH₄ in Figure 8(c); instead of reporting the normalised outlet flow rates as in Figures 4 – 6. The net outlet flow rates are calculated by subtracting the absolute volumetric flow rate of “Gas X” in the feed from the flow rate of “Gas X” in the effluent gas. A positive difference from the subtraction indicates the formation of Gas X, while a negative difference indicates the consumption of Gas X. This approach better allows for the identification of the different individual reactions possible under this CO-PrOx condition (see Equations 5 – 10) as a function temperature [9].

It is possible that CO₂ methanation (Equation 9) is an overall reaction involving the reverse WGS (Equation 10) followed by CO methanation (Equation 7) [55,62]. However, we are unable to confirm this mechanism (or any other mechanism) for CO₂ methanation based on the current experimental design. Therefore, the calculations carried out based on the GC-TCD traces implicitly assume that the methanation reactions and the reverse WGS take place in parallel during wet CO-PrOx with co-fed CO₂.



The gas feed contained 1% CO, 1% O₂, 46% H₂, 10% CO₂, 9% CO₂ and 33% N₂; which was flowed at a GHSV of 60000 mL(NTP)/g_{Co₃O₄}/hr at atmospheric pressure while heating the reactor stepwise from 100 to 450 °C. The onset of 100 °C was to prevent the condensation of water in the system. The results from the *in situ* characterisation, in terms of the cobalt phase changes and crystallite sizes, have also been included in Figures 8(a), (b) and (d), while the recorded *in situ* diffraction patterns can be found in Figure S19. Selected Rietveld refinement results (included all fitted phases) are presented in Figure S20. Only Co₃O₄/ZrO₂ and Co₃O₄/SiC were evaluated under this reaction condition as Co₃O₄/ZrO₂ exhibited the highest CO oxidation activity during dry CO-PrOx, while Co₃O₄/SiC maintained better phase stability (than Co₃O₄/ZrO₂) and good CO oxidation activity (see Figures 4 – 7, and S18). Lastly, a summary of the CO conversion and O₂ selectivity to CO₂, respectively, CO conversion to CH₄, CO₂ conversion to CH₄, CO₂ conversion to CO (*via* reverse WGS), and the magnetometry-derived DoR as a function of temperature during wet CO-PrOx with co-fed CO₂ is presented in Figure 9. For comparison, the conversions, selectivities and DoRs obtained during dry CO-PrOx are also included in Figure 9.

At temperatures below 275 °C, the oxidation of CO over the two catalysts is indicated by a positive net CO₂ outlet flow, and the negative net CO and O₂ outlet flows, respectively (see Figure 8(c)). Furthermore, the net O₂ outlet flow reaches a constant negative value, which indicates a full conversion of O₂. Similar to the dry CO-PrOx experiments, the depletion of O₂ indicates that both CO and H₂ oxidation are occurring during wet CO-PrOx with co-fed CO₂. Figure 9(a) shows that the maximum CO conversion to CO₂ is higher over Co₃O₄/ZrO₂ (73.4% at 200 °C) than over Co₃O₄/SiC (67.1% at 200 °C). The Co₃O₄/ZrO₂ catalyst also outperforms our previously reported unsupported Co₃O₄ catalyst, which achieved a maximum CO conversion of 65.3% at 200 °C under the same reaction condition [9]. However, the maximum CO conversions reported above are lower than those obtained in the absence of H₂O and CO₂ (see Figure 9(a)), and lower than the targeted conversion of 99.999% required for the purification of H₂ [10,11].

The O₂ selectivity to CO₂ of both catalysts is also lower in the presence of H₂O and CO₂ (Figure 9(b)), implying that the CO oxidation reaction is more affected than H₂ oxidation by the presence of these gas feed components. The competitive adsorption and dissociation of H₂O (reported to be more kinetically favourable than that of CO₂ [9]) on the surface of the catalysts could have led to the blockage of active sites, thus decreasing the CO oxidation activity [9,38]. This H₂O adsorption/dissociation may have also limited the occurrence of a MvK-type

mechanism for CO₂ formation from CO [9,38,66]. However, the high activity of Co₃O₄/ZrO₂ might be a result of the relatively weak interactions between Co₃O₄ and ZrO₂ support, which still allow for a more facile MvK mechanism.

The decrease in the CO oxidation activity and selectivity above 225 °C could also be a result of the catalysts reducing to CoO [5–9,58], which is confirmed by the *in situ* PXRD analysis (see Figures 8(a), 8(b) and S19). The onset formation temperature of CoO is lower for Co₃O₄/ZrO₂ (250 °C) when compared with Co₃O₄/SiC (275 °C). These onset formation temperatures are higher than those observed during dry CO-PrOx for the corresponding catalyst (Co₃O₄/ZrO₂ and Co₃O₄/SiC: 225 °C – see *in situ* PXRD results in Figures 5, 8, S15 and S19). Furthermore, the CoO phase in both catalysts is stabilised over wider temperature ranges in the presence of H₂O and CO₂ in the feed, than in the case without these feed gases. This can be mostly attributed to the presence of H₂O as it is a stronger oxidant than CO₂ [9]. In terms of crystallite sizes, the reduction of Co₃O₄ to CoO does not result in crystallite growth over both supported catalysts when H₂O and CO₂ are present in the feed (see Figure 8(b)).

Metallic Co formation over the ZrO₂- and SiC-supported catalysts is observed at higher temperatures (300 and 325 °C, respectively) in the presence of co-fed H₂O and CO₂, than in the absence of these feed gases (250 °C and 275 °C, respectively – see *in situ* PXRD and magnetometry results in Figures 5, 7 – 9, S15 and S19). Similar to CoO, the metallic Co phase forms earlier over ZrO₂ than over SiC based on magnetometry. On the other hand, PXRD analysis only shows metallic fcc Co from 400 °C over ZrO₂, while the metallic phase is not detected over SiC (see Figure 8(a)). The absence of fcc Co reflections in the Co₃O₄/SiC patterns is in-line with the relatively low DoR (13.8%) ultimately reached by this catalyst at 450 °C in the magnetometer, while a DoR of 81.1% is obtained by Co₃O₄/ZrO₂, despite PXRD suggesting a complete reduction of the oxide to the metal (see *in situ* characterisation results in Figures 8, 9 and S19). The discrepancy in the detection and quantification of fcc Co between the two *in situ* instruments may (again) be a result of their differences in sensitivity in terms of crystallite size, phase concentration and crystallinity. As proposed earlier, the nature of the Co₃O₄-SiC and CoO-SiC interactions in the SiC-supported catalyst, through the thin Si_xO_y or Si_xO_yC_z layer, may be such that the removal of lattice oxygen or the adsorption/dissociation of H₂ is kinetically hindered [48,49] when compared with the ZrO₂-supported counterpart.

The fcc Co crystallites supported on ZrO₂ are larger in size when compared with the starting Co₃O₄ crystallites (Figure 8(b)). These metallic crystallites are even larger than those formed

during dry CO-PrOx (compare crystallite sizes in Figures 5(b) and 8(b)). This indicates a much higher degree of sintering which is possibly due to the presence of co-fed H₂O, as well as the additional H₂O formed during the H₂ consuming side reactions (*vide infra*) and catalyst reduction [25,63,64].

In our previous work [9], metallic Co was responsible for the occurrence of the unwanted H₂ consuming side reactions (see Equations 6, 7, 9 and 10) under both dry and wet CO-PrOx conditions. The metallic phase was also found to be responsible for the forward WGS (Equation 8), but this reaction produces the desired H₂. In a feed containing 1% CO, 1% O₂, 46% H₂, 10% CO₂, 9% CO₂ and 33% N₂, the forward WGS is predicted to be only feasible below 285 °C based on thermodynamic calculations (equilibrium X_{CO} = 2.7% at 285 °C, with higher conversions possible below 285 °C – see Figure S21(a)). The reverse WGS is expected to take place between 290 and 450 °C (equilibrium X_{CO₂} = 25.8% at 450 °C, with lower conversions achievable below 450 °C – see Figure S21(b)) under the same gas feed. CO methanation is virtually not affected as equilibrium CO conversions above 99.0% are still possible below 450 °C (Figure S22(a)), while for CO₂ methanation, the predicted equilibrium CO₂ conversion at 450 °C is 78.6% (but higher conversions are achievable below 450 °C – Figure S22(b)). Due to the high number of reactions that are possible during wet CO-PrOx with co-fed CO₂ (see Equations 5 – 10) and the possible interconnectivity among some of them, we chose to base the thermodynamic calculations on the separate individual reactions.

The ZrO₂- and SiC-supported catalysts convert very low amounts of CO to CH₄ over metallic Co (maximum of 13.8% at 400 °C, and 8.5% at 300 °C, respectively), and show no forward WGS activity as no CO₂ is produced above 300 °C (see Figures 8(c) and 9(a)). The non-occurrence of the forward WGS is in-line with the thermodynamic predictions (Figure S21(a)). Instead, the metallic Co over ZrO₂ mostly carries out CO₂ methanation, reaching a maximum CO₂ conversion of 42.7% between 400 and 450 °C. The same catalyst also converts 3.9% of CO₂ to CO *via* the reverse WGS (Figures 8(c) and 9(c)). The SiC-supported catalyst carries out both CO₂ methanation (maximum X_{CO₂} = 20.7% at 450 °C) and the reverse WGS (maximum X_{CO₂} = 13.3% at 450 °C) over metallic Co.

The maximum conversions achieved by the catalysts during each H₂ consuming reaction are below the predicted equilibrium conversions, implying a kinetic hindrance on the progress of these reactions. The relatively high CO₂ methanation activity of the ZrO₂-supported catalyst may be attributed to the strong surface adsorption of CO₂ and the high H₂ dissociation activity

of the supported metal particles [61,62]. The small amounts of metallic Co formed over SiC may also be binding CO₂ stronger than CO since very little CO is converted to CH₄, and instead, relatively high amounts of CO₂ are converted *via* methanation and the reverse WGS. The overall low CO₂ methanation activity of the SiC-supported catalyst might be a result of its low CO₂ and H₂ dissociation activity, with the latter also causing the low DoR. These observations could be a result of the nature of the interactions between the reduced cobalt species and SiC [48,49].

In summary, the co-feeding of H₂O and CO₂ in the CO-PrOx reaction (which represents a realistic reaction environment) has a negative effect on the oxidation of CO (see Figures 9(a) and (b)). This is attributed mostly to the stronger surface adsorption of H₂O – when compared with that of CO₂ [9] – which possibly limits access to the available surface active sites, and negatively affects the MvK mechanism for CO oxidation [9,38,66]. Co-fed H₂O also increases the temperatures at which CoO and metallic Co are formed; and decreases the DoR to the metallic phase (relative to the formation temperatures and DoRs observed during dry CO-PrOx – see Figures 5, 8 and 9) due to its strong oxidising nature [9]. The presence of CO₂ in the feed leads to the undesired increase in the H₂ conversion (when compared with dry CO-PrOx) *via* CO and CO₂ methanation, and the reverse WGS over metallic Co (see Figure 9(c)) [9].

The relatively weak NPSI thought to be present in Co₃O₄/ZrO₂ allow for higher CO conversions to CO₂ than those observed with the Co₃O₄/SiC catalyst in the presence of co-fed H₂O and CO₂ (Figure 9(a)). However, the weak interactions may have also caused the undesired earlier reduction of Co₃O₄ to CoO and metallic Co over ZrO₂ than over SiC (Figures 8 and 9). The high CO oxidation activity and bulk reducibility of Co₃O₄ realised over ZrO₂, when compared with SiC, was also observed during dry CO-PrOx. Therefore, the work presented in this section also emphasises the importance of having a bi-functional support that would enhance the catalytic performance and phase stability, as also mentioned in section 3.3.1.

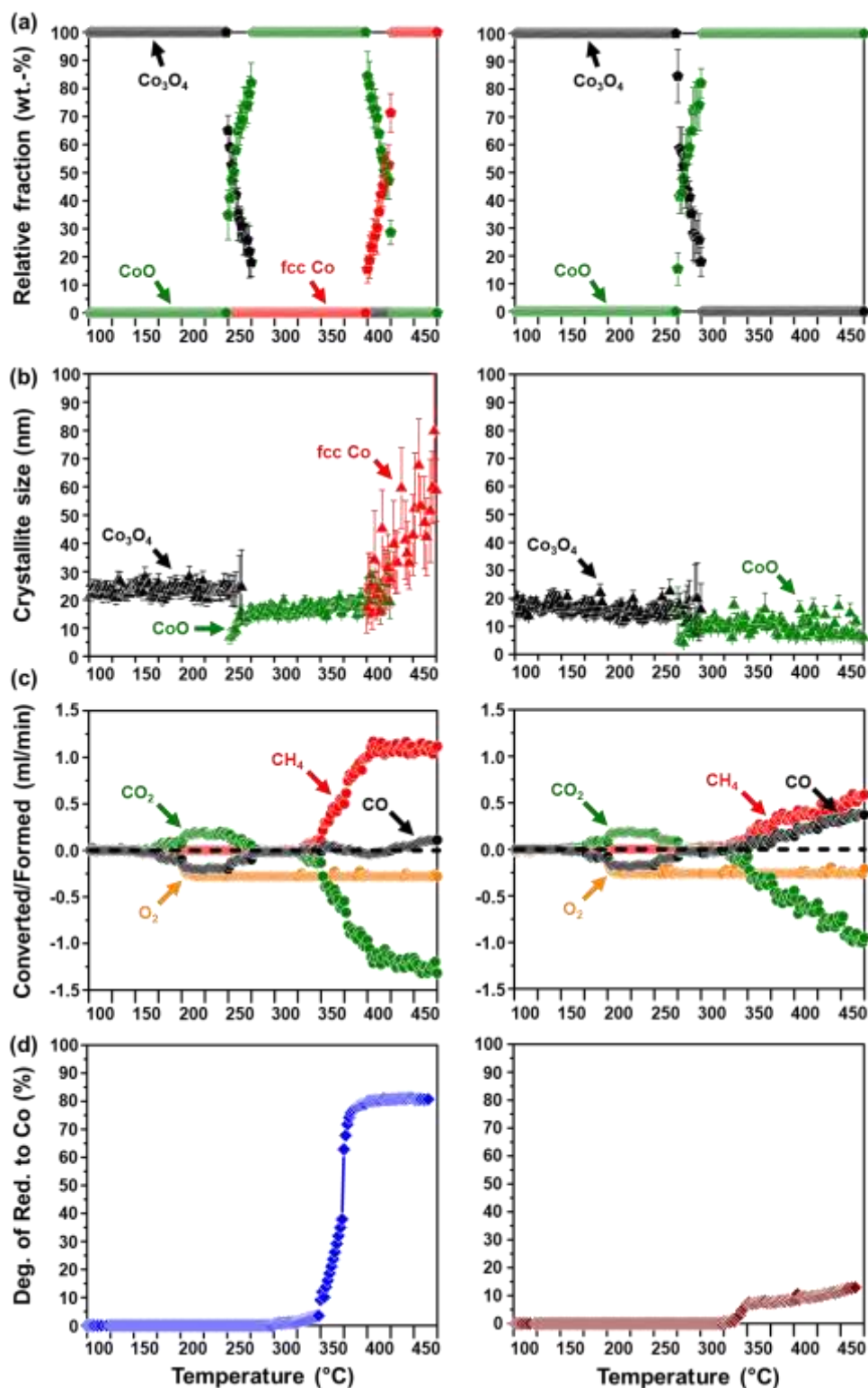


Figure 8: (a) PXRD-derived relative weight fractions, and (b) average crystallite sizes of the different Co-based phases formed (excluding the supports), (c) net outlet flow rates of CO, O₂, CO₂ and CH₄; as well as the (d) magnetometry-derived DoR of Co₃O₄ to metallic Co for (*left*) Co₃O₄/ZrO₂, and (*right*) Co₃O₄/SiC. (Feed composition: 1% CO, 1% O₂, 46% H₂, 10% H₂O, 9% CO₂ and 33% N₂; pressure: atmospheric, GHSV: 60000 mL(NTP)/gCo₃O₄/hr).

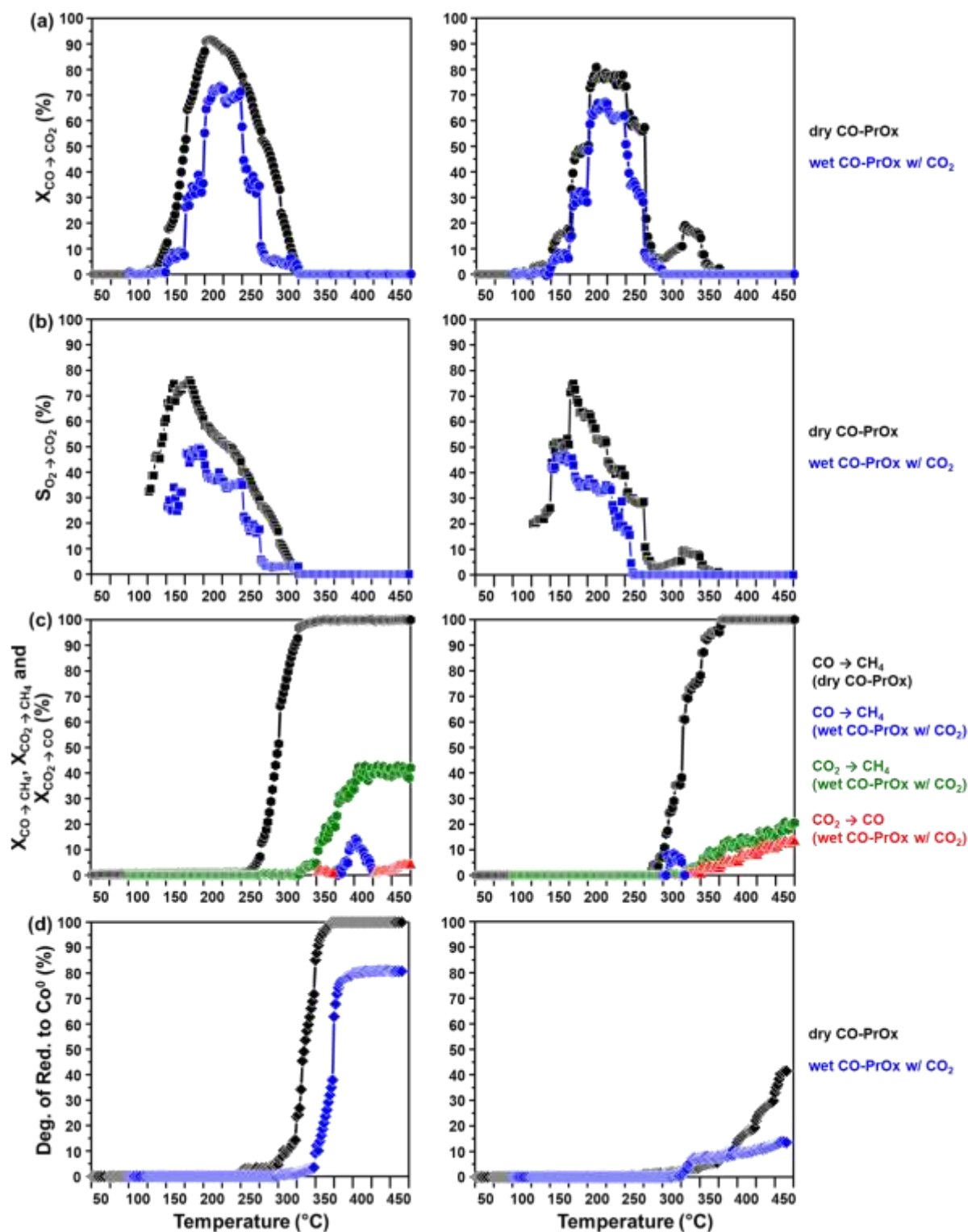


Figure 9: (a) CO conversion to CO_2 ($X_{\text{CO} \rightarrow \text{CO}_2}$), and (b) O_2 selectivity to CO_2 ($S_{\text{O}_2 \rightarrow \text{CO}_2}$). (c) CO conversion to CH_4 ($X_{\text{CO} \rightarrow \text{CH}_4}$), CO_2 conversion to CH_4 ($X_{\text{CO}_2 \rightarrow \text{CH}_4}$), and CO_2 conversion to CO ($X_{\text{CO}_2 \rightarrow \text{CO}}$), respectively. (d) Magnetometry-derived DoR of Co_3O_4 to metallic Co during dry and wet CO-PrOx over (left) $\text{Co}_3\text{O}_4/\text{ZrO}_2$, and (right) $\text{Co}_3\text{O}_4/\text{SiC}$. The O_2 selectivity to CO_2 was calculated at temperatures where both CO and O_2 were converted (see Figures 5(c), 7(a), 8(c) and 9(a)).

3.4. *Ex situ* characterisation of spent catalysts: XAS and STEM-EELS analysis

The spent catalysts recovered after the dry and wet CO-PrOx experiments performed in the magnetometer, were analysed using *ex situ* XAS primarily to determine if there were any metal-support compounds (such as Co_2SiO_4 and CoAl_2O_4) present in the spent samples. *Ex situ* STEM-EELS analysis was performed to determine any significant size changes of the Co-bearing particles as a result of the applied reaction conditions. Due to the long storage times (6 to 12 months) of the samples in a non-inert environment at room temperature, between the time they were recovered from the magnetometer and the time they were analysed using XAS and STEM-EELS, respectively, re-oxidation of the previously formed CoO and/or metallic Co was expected. However, this is not a concern as these phases have been adequately detected and quantified using PXRD and magnetometry. The size of the previously formed CoO and metallic Co can be expected to increase up to 4% and 17 – 20%, respectively, depending on the degree of re-oxidation (see Equations 2 – 4).

The presence of metal-support compounds could not be confirmed using the magnetometer since these are paramagnetic within the temperature range chosen for the reactions [35–37], while PXRD did not show any evidence for the presence of such crystalline bulk material. It may still be possible that these species were formed in some of the samples but in amounts that are below the intrinsic detection limit of the current PXRD instrument, and/or formed as amorphous phases. Therefore, should these compounds have formed during dry or wet CO-PrOx, they would remain stable even during the long storage periods leading to their analysis using XAS and STEM-EELS [25,67].

Figure 10(a) shows the normalised XANES spectra of the reference compounds, *viz.*, Co_3O_4 , CoO, Co_2SiO_4 , CoAl_2O_4 and metallic Co. Figures 10((b) – (f)) display the normalised spectra of the supported spent samples, and the obtained results from the LCF. Table 3 summarises the relative fraction of the different Co-based phases detected in each sample and the corresponding R-factor for each LCF performed. The R-factor is a metric for judging misfit in the LCF, with values very close to zero indicating minor or no misfits [68].

The normalised XANES spectrum of the CeO_2 -supported spent sample mostly exhibits features of CoO, but the LCF results also indicate the presence of small amounts of Co_3O_4 and metallic Co (see Table 3). There seems to be an additional phase present in the spent sample as indicated by the slight misfit in the LCF (see Figure 10(b), and the normalised first derivative XANES

spectrum in Figure S23(b)), as well as the relatively high R-factor of 0.081 (Table 3). From the conventional H₂-TPR results (Figure 3(b)), there was a peak assigned to the possible reduction of Co-Ce oxide species at 450 °C [55,56]. This was also proposed during the magnetometry-based dry CO-PrOx reaction, together with the possibility of CoO_{1-x} encapsulation by partially reduced ceria species [57]. Therefore, the misfit in the LCF may be due to the presence of some Co_xCe_yO_z species that formed under the reducing CO-PrOx environment which, at this stage, cannot be adequately identified using XAS.

The spectrum of the spent ZrO₂-supported catalyst after dry CO-PrOx (Figure 10(c)) resembles that of the Co₃O₄ reference, with the LCF results also indicating the presence of small amounts of CoO (Table 3). Since the *in situ* characterisation results indicated a DoR of 100% to metallic Co for this catalyst, the oxides present in the Co₃O₄/ZrO₂ spent sample are a result of re-oxidation of the metal during sample storage prior to the XAS measurements. The XANES of the spent ZrO₂-supported catalyst after wet CO-PrOx with co-fed CO₂ (Figure 11(a)) exhibits the typical metallic pre-edge feature at 7710 eV and a relatively intense white line feature between 7726 and 7729 eV, possibly indicating the presence of CoO and Co₃O₄. The less intense features from 7729 to 7825 eV further indicate that the sample has mostly metallic species. A lower degree of re-oxidation of the metallic phase took place in this spent sample (when compared with the spent sample obtained after dry CO-PrOx) as a relative metallic Co concentration of $46.0 \pm 0.4\%$ is estimated from the LCF, while a DoR of 81.1% was calculated from the magnetometry data. The lower degree of re-oxidation of the sample obtained after wet CO-PrOx with co-fed CO₂ could be a result of its relatively short storage duration prior to the XAS measurements.

In the XANES spectrum of the spent Co₃O₄/SiC catalyst after dry CO-PrOx (Figure 10(d)), there is a pre-edge feature at 7710 eV which also suggests the presence of metallic Co. The pronounced white line feature at 7726 eV indicates the presence of CoO. The less intense features between 7726 and 7825 eV correspond to those found in the spectrum of the CoO and metallic Co reference samples, respectively. The estimated relative metallic Co fraction ($40.9 \pm 0.5\%$) in this spent sample also agrees with the calculated DoR (41.5%) from the magnetometry data at 450 °C (Figures 5((d), *right*) and 7(d)). This suggests that the metallic phase was virtually not re-oxidised during sample storage. The XANES of the SiC-supported spent catalyst obtained after wet CO-PrOx with co-fed CO₂ (Figure 11(b)) displays features similar to those of CoO between 7700 and 7825 eV. However, based on the LCF results, there is also $14.6 \pm 0.5\%$ metallic Co, which is very close to the DoR of 13.8% calculated from the

magnetometry data at 450 °C (Figures 8((d), *right*) and 9((d), *right*)). Similar to the spent sample obtained under the dry condition, the metallic Co after wet CO-PrOx was virtually not re-oxidised.

The SiC support has a 1 – 2 nm Si_xO_y or $\text{Si}_x\text{O}_y\text{C}_z$ layer around the core particles of the support (see Figure S14(b)), which possibly interacts relatively strongly with Co-based oxide species, hence, the low DoRs obtained under dry and wet CO-PrOx conditions. However, the LCF in Figures 10(d) and 11(b) does not show evidence for a cobalt silicate-like phase ($\text{Co}_x\text{Si}_y\text{O}_z$) being present, implying that this thin Si_xO_y or $\text{Si}_x\text{O}_y\text{C}_z$ layer does not react with the cobalt species.

The $\text{Co}_3\text{O}_4/\text{SiO}_2$ spent sample (Figure 10(e)) is mostly composed of the CoO phase, but small amounts of Co_3O_4 , Co_2SiO_4 and metallic Co are confirmed by the LCF (Table 3). The formation of Co_2SiO_4 ($7.7 \pm 0.3\%$) during dry CO-PrOx possibly suggests that the nature and/or strength of the NPSI may have caused for some small amounts of $\text{Co}^{\text{n+}}$ species to react with the SiO_2 [13,14,25]. The presence of $3.7 \pm 0.9\%$ metallic Co indicates re-oxidation during storage, as this sample had reached a DoR of 22.1% at 450 °C during the *in situ* magnetometry experiments.

The spectrum of the $\text{Co}_3\text{O}_4/\text{Al}_2\text{O}_3$ spent sample (Figure 10(f)) exhibits features similar to those in the spectrum of the CoO reference. However, the LCF suggests that Co_3O_4 and CoAl_2O_4 may also be present in the spent sample. The metallic phase was not detected due to re-oxidation, but the magnetometry studies showed that this sample reached the lowest DoR of 16.2% at 450 °C during dry CO-PrOx when compared with the other catalysts. This very low DoR and the formation of relatively high amounts of CoAl_2O_4 ($26.6 \pm 1.6\%$) possibly indicates the existence of very strong NPSI, which prevented the reduction of some cobalt oxide species to Co^0 , and instead, enabled the reaction of these species with the Al_2O_3 support [14,18,24,25]. There is a slight misfit of the LCF in Figure 10(f) (also see first derivative XANES spectrum in Figure S23(c)), which is also indicated by a relatively high R-factor of 0.021 (Table 3). At this stage, we propose that this may be due to the presence of an additional cobalt aluminate phase with a Co:Al:O molar ratio that is not 1:2:4 [67].

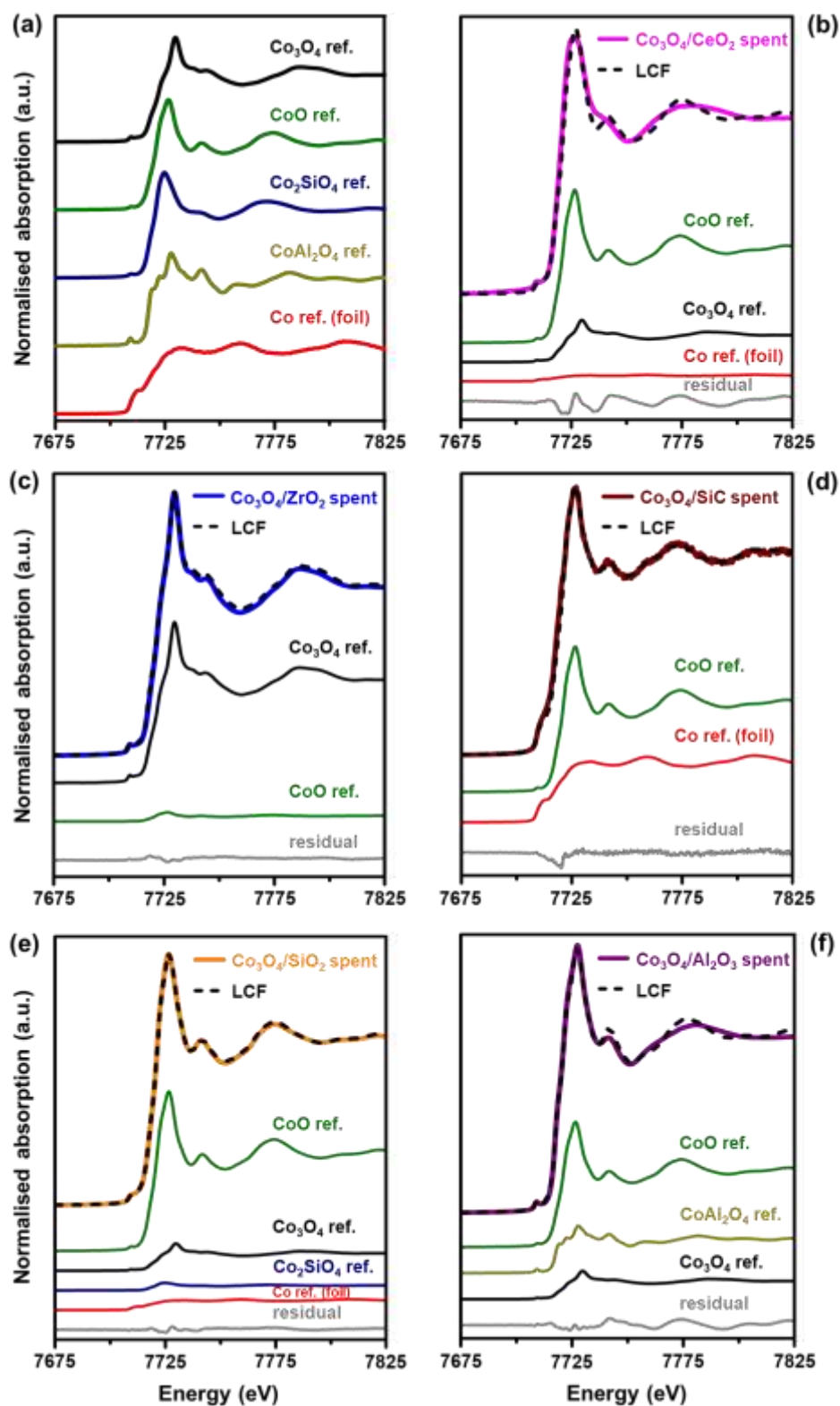


Figure 10: (a) Normalised XANES spectra of the reference compounds Co_3O_4 , CoO , Co_2SiO_4 , CoAl_2O_4 and Co foil. (b) – (f) Normalised XANES spectra of the spent catalysts obtained after dry CO-PrOx , together with the resulting LCF of the spectral components in each sample. The reference spectra in (b) – (f) are scaled in accordance with their contribution in the LCF.

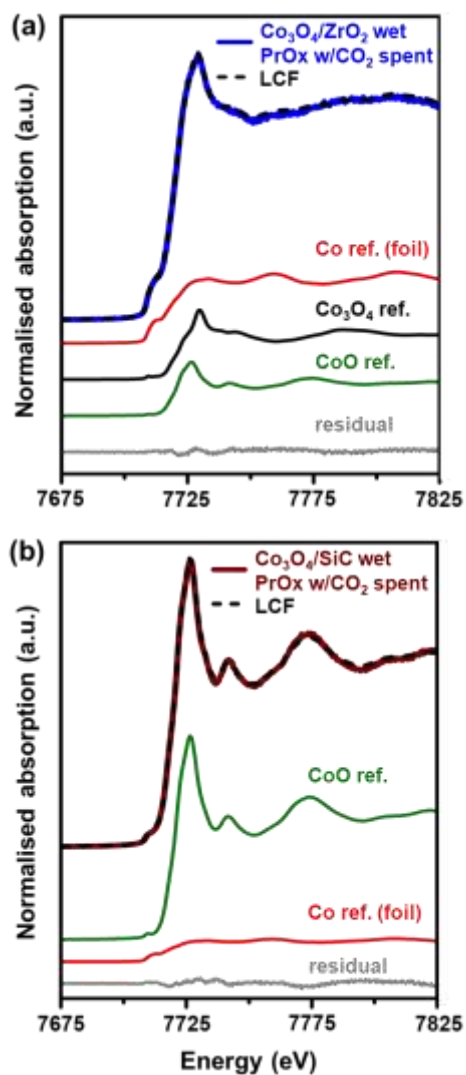


Figure 11: Normalised XANES spectrum of the spent (a) $\text{Co}_3\text{O}_4/\text{ZrO}_2$, and (b) $\text{Co}_3\text{O}_4/\text{SiC}$ catalyst obtained after wet CO-PrOx with co-fed CO_2 , together with the resulting LCF of the spectral components in each sample. The reference spectra in (a) and (b) are scaled in accordance with their contribution in the LCF.

Table 3: Summary of the results obtained after performing a linear combination fit of the normalised XANES spectra.

Sample name	Co ₃ O ₄ (%)	CoO (%)	Co _a M _x O _{y+a} (%)*	Co ⁰ (%)	R-factor (-)
Co ₃ O ₄ /CeO ₂ spent ^{§, #}	21.4 ± 1.5	73.8 ± 2.3	-	4.7 ± 1.2	0.081
Co ₃ O ₄ /ZrO ₂ spent [§]	94.9 ± 0.6	5.1 ± 0.9	-	-	0.003
Co ₃ O ₄ /SiC spent	-	59.1 ± 1.1	-	40.9 ± 0.5	0.004
Co ₃ O ₄ /SiO ₂ spent	13.5 ± 2.0	75.1 ± 0.9	7.7 ± 0.3	3.7 ± 0.9	0.001
Co ₃ O ₄ /Al ₂ O ₃ spent	14.1 ± 1.9	59.3 ± 1.0	26.6 ± 1.6	-	0.021
Co ₃ O ₄ /ZrO ₂ _wet CO-PrOx w/ CO ₂ spent [§]	31.2 ± 0.7	22.8 ± 0.4	-	46.0 ± 0.4	0.001
Co ₃ O ₄ /SiC_wet CO-PrOx w/ CO ₂ spent	-	85.4 ± 0.4	-	14.6 ± 0.5	0.001

* Co_aM_xO_{y+a}: M = Si or Al, a = 1 or 2, x = 1 or 2 and y = 2 or 3 for Co₂SiO₄ and CoAl₂O₄.

§ there are no known or well characterised Co-Ce or Co-Zr oxides.

there may be some unknown Co-Ce oxidic or metallic phase present that was not included in the LCF.

Note: The “-” indicates the (probable) absence of a particular Co-based phase in the spent sample according to the LCF.

Figure 12 shows the STEM-EELS micrographs for the Co₃O₄/Al₂O₃ spent sample. The composite map in Figure 12(b) shows a number of yellow regions, while the aluminium map in Figure 12(c) shows a number of regions with a brighter shade of red (see annotations on the map). These bright red regions are also where the cobalt species are located (see composite map in Figure 12(b), and the cobalt map in Figure 12(c)). Therefore, the brighter red regions in the aluminium map and the yellow regions in the composite map indicate some degree of chemical mixing between the species of Al and Co. This could be a result of the strong interaction between the Al₂O₃ support and the Co-bearing nanoparticles, as well as a result of the reaction conditions (*i.e.*, temperature and the presence of H₂/H₂O) [14,18,24,25]. Due to the extent of the chemical mixing, there were very few distinct Co-bearing nanoparticles that could be identified and considered for obtaining a particle size distribution. Nonetheless, this observation is in good agreement with the XAS results that revealed the existence of CoAl₂O₄ (and possibly other Co_xAl_yO_z species) in this spent sample (Figure 10(f)).

The STEM-EELS micrographs of the other spent catalysts (Figures S24 – S26) do not show evidence of chemical mixing between the Co species and the species from each support, *i.e.*,

evidence of metal-support compound formation. However, there are areas of the supports that show atomically distributed Co (or support “wetting” by Co species), which may indicate some significant interactions between the Co species and each of the supports. There also exists distinct Co-bearing particles over most of the supports which are similar or smaller in size when compared with the sizes obtained from the *in situ* PXRD analysis (see Figures 5(b), 6(b) and 8(b)). However, the Co-bearing particles supported on ZrO₂, obtained after dry and wet CO-PrOx, respectively, appear to be significantly smaller than the sizes estimated using Rietveld refinement. At this stage, this discrepancy is not completely understood, but it may be possible that there are some large particles in these spent samples that were not observed during STEM-EELS analysis due to their low count relative to the smaller particles. These large particles would be detectable using PXRD and would increase the volume-based average size estimated using Rietveld refinement due to them having a larger absolute volume [43].

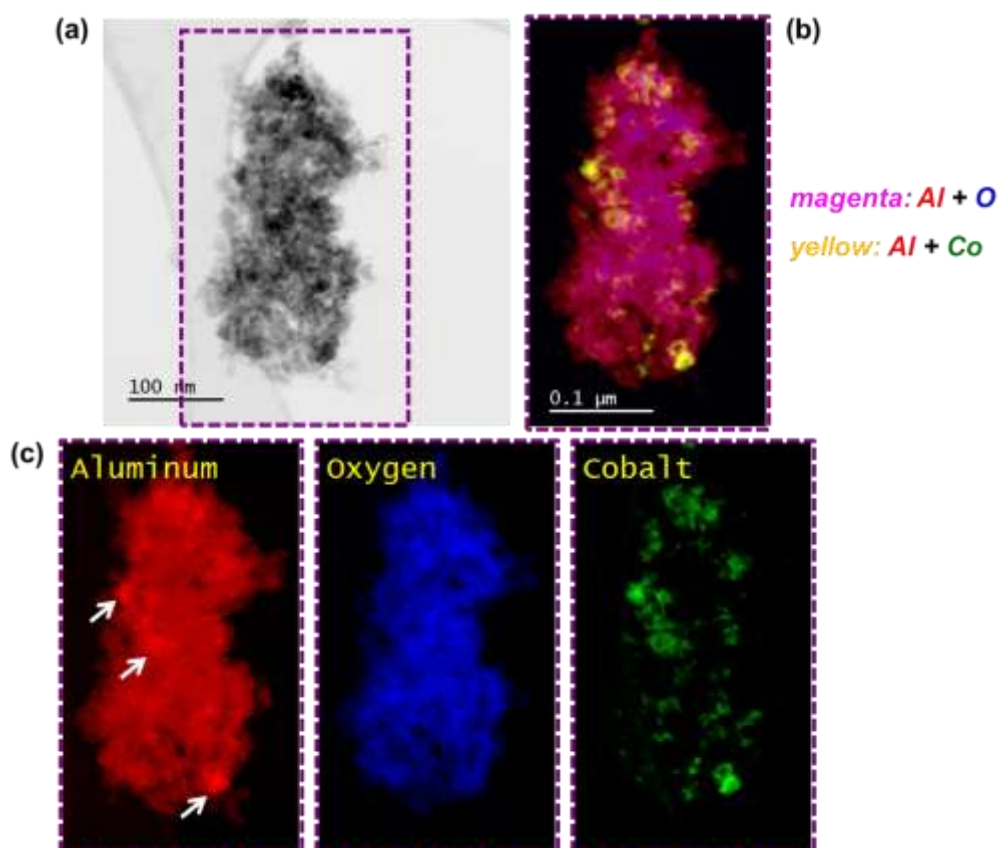


Figure 12: (a) Bright-field STEM image of the spent Co₃O₄/Al₂O₃ catalyst obtained after dry CO-PrOx. (b) Magnified composite STEM-EELS elemental map showing the regions with Al, O and Co. (c) Corresponding magnified STEM-EELS maps of the individual elements. The white arrows on the Al map show the bright regions which are thought to be the Al species that are chemically mixed with Co.

Summary and Conclusion

The current study aimed at reporting the effect of various support materials (CeO_2 , ZrO_2 , SiC , SiO_2 and Al_2O_3) and the gas environment on the preferential oxidation of CO, in the context of H_2 purification for PEMFCs. The use of in-house developed *in situ* techniques proved very crucial in investigating the phase changes of the catalysts and in understanding the effects of these changes on the CO oxidation activity and selectivity. We have demonstrated that weak nanoparticle-support interactions (NPSI) are beneficial, as these ensure high CO conversions to CO_2 *via* the well accepted Mars-van Krevelen mechanism, which requires the catalyst to be reducible (ideally on the surface). However, the weak NPSI have a negative effect on the phase stability of bulk Co_3O_4 , as this phase can ultimately reduce to metallic Co, which is highly selective to undesired H_2 consuming reactions (*viz.*, H_2 oxidation, CO/ CO_2 methanation and the reverse WGS).

The ZrO_2 -supported catalyst proved to be superior in terms of CO oxidation activity – achieving the highest maximum CO conversion to CO_2 of 91.5% under the dry CO-PrOx condition, and 73.4% under the wet condition involving H_2O and CO_2 co-feeding. However, the same catalyst reached the highest DoR to metallic Co (*i.e.*, 100% under the dry condition, and 81.1% under the wet condition at 450 °C) of all evaluated catalysts. The decrease in the CO conversion to CO_2 and the DoR under the wet CO-PrOx condition is possibly a result of the competitive adsorption and dissociation of H_2O on the catalyst surface, which blocks access to active sites, and the oxidative nature of H_2O , which slows down reduction. The co-fed CO_2 under the wet CO-PrOx condition was mostly converted to CH_4 over the metallic phase supported on ZrO_2 , with small amounts of CO_2 also converted to CO *via* reverse WGS. On the other hand, $\text{Co}_3\text{O}_4/\text{SiC}$ displayed low H_2 dissociation activity, which resulted in the low DoR, low CO_2 methanation activity and relatively high reverse WGS activity when compared with $\text{Co}_3\text{O}_4/\text{ZrO}_2$.

The overall high CO oxidation activity and Co_3O_4 reducibility of the ZrO_2 -supported catalyst may be attributed to the existence of weak NPSI. The least CO oxidation active $\text{Co}_3\text{O}_4/\text{Al}_2\text{O}_3$ catalyst was also the least reducible and the least methanation active catalyst. This was attributed to the possible existence of very strong NPSI in this catalyst. This further resulted in the undesired loss of cobalt oxide species *via* the formation CoAl_2O_4 ($26.6 \pm 1.6\%$) under the varying partial pressure ratios of $\text{H}_2:\text{H}_2\text{O}$ realised during CO-PrOx. Therefore, for the first time,

this study has shown the bi-functional role required of support materials, *i.e.*, to enhance CO oxidation activity and selectivity, while stabilising the Co_3O_4 phase over a wide temperature range during CO-PrOx.

CRedit Author Contribution Statement

Author 1, Thulani M. Nyathi: Conceptualisation, Methodology, Investigation, Formal Analysis, Visualization, Writing – Original Draft, Writing – Review & Editing.

Author 2, Mohamed I. Fadlalla: Methodology, Investigation, Writing – Review & Editing.

Author 3, Nico Fischer: Co-supervision, Conceptualisation, Writing – Review & Editing.

Author 4, Andrew P. E. York: Co-supervision, Funding Acquisition, Conceptualisation, Writing – Review & Editing.

Author 5, Ezra J. Olivier: Methodology, Investigation, Formal Analysis, Writing – Review & Editing.

Author 6, Emma K. Gibson: Methodology, Investigation, Formal Analysis, Writing – Review & Editing.

Author 7, Peter P. Wells: Funding Acquisition, Methodology, Writing – Review & Editing.

Author 8, Michael Claeys: Supervision, Funding Acquisition, Conceptualisation, Methodology, Project Administration, Resources, Writing – Review & Editing.

Declaration of interests

The authors declare that they have no known competing financial interests or personal relationships that could have appeared to influence the work reported in this paper.

Acknowledgements

The financial support from Johnson Matthey, the DSI-NRF Centre of Excellence in Catalysis (*c*change*), and the Science and Technology Facilities Council (STFC) *via* GCRF-START (Global Challenges Research Fund – Synchrotron Techniques for African Research and Technology (ST/R002754/1)) is gratefully acknowledged. The authors would also like to thank

Ms. Zulfa le Riche (from the University of Cape Town) for carrying out the ICP-OES analysis. Finally, Dr. Nitya Ramanan (from Diamond Light Source) and Mr. Monik Panchal (from the UK Catalysis Hub) are thanked for assisting with the XAS measurements on beamline B18 at Diamond Light Source (sessions: SP19850-3, SP19850-4, SP19850-5).

References

- [1] V. Iablokov, R. Barbosa, G. Pollefeyt, I. Van Driessche, S. Chenakin, N. Kruse, *ACS Catal.* 5 (2015) 5714–5718.
- [2] Y. Teng, Y. Kusano, M. Azuma, M. Haruta, Y. Shimakawa, *Catal. Sci. Technol.* 1 (2011) 920–922.
- [3] C.-B. Wang, C.-W. Tang, S.-J. Gau, S.-H. Chien, *Catal. Lett.* 101 (2005) 59–63.
- [4] C.-B. Wang, C.-W. Tang, H.-C. Tsai, S.-H. Chien, *Catal. Lett.* 107 (2006) 223–230.
- [5] L. Lukashuk, K. Föttinger, E. Kolar, C. Rameshan, D. Teschner, M. Hävecker, A. Knop-Gericke, N. Yigit, H. Li, E. McDermott, M. Stöger-Pollach, G. Rupprechter, *J. Catal.* 344 (2016) 1–15.
- [6] T.M. Nyathi, N. Fischer, A.P.E. York, M. Claeys, *Faraday Discuss.* 197 (2017) 269–285.
- [7] M. Khasu, T. Nyathi, D.J. Morgan, G.J. Hutchings, M. Claeys, N. Fischer, *Catal. Sci. Technol.* 7 (2017) 4806–4817.
- [8] T.M. Nyathi, N. Fischer, A.P.E. York, D.J. Morgan, G.J. Hutchings, E.K. Gibson, P.P. Wells, C.R.A. Catlow, M. Claeys, *ACS Catal.* 9 (2019) 7166–7178.
- [9] T.M. Nyathi, N. Fischer, A.P.E. York, M. Claeys, *ACS Catal.* 10 (2020) 11892–11911.
- [10] T.V. Choudhary, D.W. Goodman, *Catal. Today* 77 (2002) 65–78.
- [11] A. Mishra, R. Prasad, *Bull. Chem. React. Eng. Catal.* 6 (2011) 1–14.
- [12] R.C. Reuel, C.H. Bartholomew, *J. Catal.* 85 (1984) 78–88.
- [13] E. van Steen, G.S. Sewell, R.A. Makhothe, C. Micklethwaite, H. Manstein, M. de Lange, C.T. O’Connor, *J. Catal.* 162 (1996) 220–229.
- [14] G. Jacobs, T.K. Das, Y. Zhang, J. Li, G. Racoillet, B.H. Davis, *Appl. Catal. A* 233 (2002) 263–281.
- [15] Z. Zhao, M.M. Yung, U.S. Ozkan, *Catal. Commun.* 9 (2008) 1465–1471.
- [16] N. Fischer, M. Minnermann, M. Baeumer, E. van Steen, M. Claeys, *Catal. Lett.* 142 (2012) 830–837.
- [17] L.J. Garces, B. Hincapie, R. Zerger, S.L. Suib, *J. Phys. Chem. C* 119 (2015) 5484–5490.
- [18] N.E. Tsakoumis, R.E. Johnsen, W. van Beek, M. Rønning, E. Rytter, A. Holmen, *Chem.*

- Commun. 52 (2016) 3239–3242.
- [19] P. Mars, D.W. van Krevelen, Chem. Eng. Sci. 3 (1954) 41–59.
- [20] D. Perti, R.L. Kabel, G.J. McCarthy, AIChE J. 31 (1985) 1435–1440.
- [21] L. Lukashuk, N. Yigit, R. Rameshan, E. Kolar, D. Teschner, M. Hävecker, A. Knop-Gericke, R. Schlögl, K. Föttinger, G. Rupprechter, ACS Catal. 8 (2018) 8630–8641.
- [22] L.E. Gómez, A. V. Boix, E.E. Miró, Catal. Today 216 (2013) 246–253.
- [23] A. Jha, Y.-L. Lee, W.-J. Jang, J.-O. Shim, K.-W. Jeon, H.-S. Na, H.-M. Kim, H.-S. Roh, D.-W. Jeong, S.G. Jeon, J.-G. Na, W.L. Yoon, Mol. Catal. 433 (2017) 145–152.
- [24] N.E. Tsakoumis, J.C. Walmsley, M. Rønning, W. van Beek, E. Rytter, A. Holmen, J. Am. Chem. Soc. 139 (2017) 3706–3715.
- [25] M. Wolf, E.K. Gibson, E.J. Olivier, J.H. Neethling, C.R.A. Catlow, N. Fischer, M. Claeys, ACS Catal. 9 (2019) 4902–4918.
- [26] P. Nguyen, C. Pham, Appl. Catal. A 391 (2011) 443–454.
- [27] M.C.M. Claeys, N.F. Fischer, Sample Presentation Device for Radiation-Based Analytical Equipment, US Patent 8,597,598 B2, 2013.
- [28] N. Fischer, M. Claeys, Catal. Today 275 (2016) 149–154.
- [29] N. Fischer, M. Claeys, J. Phys. D. Appl. Phys. 53 (2020) 293001.
- [30] M.C.M. Claeys, E.W.J. van Steen, J.L. Visagie, J. van de Loosdrecht, Magnetometer, US Patent 8,773,118 B2, 2014.
- [31] P. Munnik, N.A. Krans, P.E. de Jongh, K.P. de Jong, ACS Catal. 4 (2014) 3219–3226.
- [32] ICDD PDF-2 Release 2008 (Database), International Centre for Diffraction Data, Newtown Square, PA, USA, 2008.
- [33] A.A. Coelho, J. Appl. Crystallogr. 36 (2003) 86–95.
- [34] V. Sechovský, in: K.H.J. Buschow, R.W. Cahn, M.C. Flemings, B. Ilshner, E.J. Kramer, S. Mahajan, P. Veyssièrè (Eds.), Encycl. Mater. Sci. Technol., 2nd ed., Elsevier Science Ltd, 2001, pp. 5018–5032.
- [35] C.G. Shull, W.A. Strauser, E.O. Wollan, Phys. Rev. 83 (1951) 333–345.
- [36] S. Nomura, R. Santoro, J. Fang, R. Newnham, J. Phys. Chem. Solids 25 (1964) 901–905.
- [37] W.L. Roth, J. Phys. 25 (1964) 507–515.
- [38] Q. Guo, Y. Liu, React. Kinet. Catal. Lett. 92 (2007) 19–25.
- [39] T. Cwele, N. Mahadevaiah, S. Singh, H.B. Friedrich, Appl. Catal. B 182 (2016) 1–14.
- [40] NIST: X-Ray Mass Attenuation Coefficients - Table 3.

<https://physics.nist.gov/PhysRefData/XrayMassCoef/tab3.html>. (accessed May 2021).

- [41] A.A. Adesina, *Appl. Catal. A* 138 (1996) 345–367.
- [42] E. Marceau, X. Carrier, M. Che, O. Clause, C. Marcilly, in: G. Ertl, H. Knözinger, F. Schüth, J. Weitkamp (Eds.), *Handb. Heterog. Catal.*, Wiley-VCH Verlag GmbH & Co. KGaA, Weinheim, Germany, 2008, pp. 467–484.
- [43] C. Weidenthaler, *Nanoscale* 3 (2011) 792–810.
- [44] H.E. du Plessis, J.P.R. de Villiers, A. Tuling, E.J. Olivier, *Phys. Chem. Chem. Phys.* 18 (2016) 30183–30188.
- [45] S.W.T. Price, D.J. Martin, A.D. Parsons, W.A. Sławiński, A. Vamvakeros, S.J. Keylock, A.M. Beale, J.F.W. Mosselmans, *Sci. Adv.* 3 (2017) e1602838.
- [46] E. Klugmann, H.J. Blythe, F. Walz, *Phys. Status Solidi* 146 (1994) 803–813.
- [47] S. Ram, *Mater. Sci. Eng. A* 304–306 (2001) 923–927.
- [48] B. Delmon, in: G. Ertl, H. Knözinger, J. Weitkamp (Eds.), *Prep. Solid Catal.*, Wiley-VCH Verlag GmbH, Weinheim, Germany, 1999, pp. 541–579.
- [49] T.W. van Deelen, C. Hernández Mejía, K.P. de Jong, *Nat. Catal.* 2 (2019) 955–970.
- [50] E. van Steen, M. Claeys, M.E. Dry, J. van de Loosdrecht, E.L. Viljoen, J.L. Visagie, *J. Phys. Chem. B* 109 (2005) 3575–3577.
- [51] N. Fischer, E. van Steen, M. Claeys, *Catal. Today* 171 (2011) 174–179.
- [52] A. Moen, D.G. Nicholson, B.S. Clausen, P.L. Hansen, A. Molenbroek, G. Steffensen, *Chem. Mater.* 9 (1997) 1241–1247.
- [53] B. Ernst, A. Bensaddik, L. Hilaire, P. Chaumette, A. Kiennemann, *Catal. Today* 39 (1998) 329–341.
- [54] H.C. Yao, Y.F. Yu Yao, *J. Catal.* 86 (1984) 254–265.
- [55] L. Wang, H. Liu, *Catal. Today* 316 (2018) 155–161.
- [56] Y. Cao, X. Peng, Z. Tan, Y. Liu, X. Wang, W. Zhao, L. Jiang, *Ind. Eng. Chem. Res.* 58 (2019) 17692–17698.
- [57] S. Bernal, J.J. Calvino, M.A. Cauqui, J.M. Gatica, C. Larese, J.A. Pérez Omil, J.M. Pintado, *Catal. Today* 50 (1999) 175–206.
- [58] L. Lukashuk, N. Yigit, H. Li, J. Bernardi, K. Föttinger, G. Rupprechter, *Catal. Today* 336 (2019) 139–147.
- [59] D. Gamarra, C. Belver, M. Fernández-García, A. Martínez-Arias, *J. Am. Chem. Soc.* 129 (2007) 12064–12065.
- [60] B. Roldan Cuenya, F. Behafarid, *Surf. Sci. Rep.* 70 (2015) 135–187.

- [61] W. Li, X. Nie, X. Jiang, A. Zhang, F. Ding, M. Liu, Z. Liu, X. Guo, C. Song, *Appl. Catal. B* 220 (2018) 397–408.
- [62] X. Nie, H. Wang, W. Li, Y. Chen, X. Guo, C. Song, *J. CO₂ Util.* 24 (2018) 99–111.
- [63] G.L. Bezemer, T.J. Remans, A.P. van Bavel, A.I. Dugulan, *J. Am. Chem. Soc.* 132 (2010) 8540–8541.
- [64] M. Claeys, M.E. Dry, E. van Steen, P.J. van Berge, S. Booyens, R. Crous, P. van Helden, J. Labuschagne, D.J. Moodley, A.M. Saib, *ACS Catal.* 5 (2015) 841–852.
- [65] R.A. van Santen, *Acc. Chem. Res.* 42 (2009) 57–66.
- [66] F. Zasada, W. Piskorz, S. Cristol, J.F. Paul, A. Kotarba, Z. Sojka, *J. Phys. Chem. C* 114 (2010) 22245–22253.
- [67] M. Wolf, S.J. Roberts, W. Marquart, E.J. Olivier, N.T.J. Luchters, E.K. Gibson, C.R.A. Catlow, J.H. Neethling, N. Fischer, M. Claeys, *Dalt. Trans.* 48 (2019) 13858–13868.
- [68] B. Ravel, in: J.A. van Bokhoven, C. Lamberti (Eds.), *X-Ray Absorpt. X-Ray Emiss. Spectrosc.*, John Wiley & Sons, Ltd, Chichester, UK, 2016, pp. 281–302.